Eco-evolutionary dynamics of sea star wasting disease: An individual-based model for *Pycnopodia helianthoides* conservation

Willem Weertman[1,2]

[1]Department of Psychology, University of Washington, Seattle, WA, USA
[2]Friday Harbor Laboratories, University of Washington, Friday Harbor, WA, USA

Abstract

Sea star wasting disease (SSWD) caused a >90% decline in the sunflower sea star (*Pycnopodia helianthoides*), a keystone predator in northeastern Pacific kelp forest ecosystems, triggering cascading trophic effects including sea urchin population explosions and extensive kelp deforestation. Despite ongoing captive breeding and experimental outplanting, no predictive framework integrates disease dynamics, host genetics, and spatial structure to evaluate reintroduction outcomes under continued disease pressure. Here we present SSWD-EvoEpi, the first coupled eco-evolutionary epidemiological individual-based model for *P. helianthoides* and SSWD, parameterized following confirmation of *Vibrio pectenicida* as a causative agent. The model tracks individual sea stars carrying diploid genotypes across 51 loci encoding three heritable defense traits—resistance (immune exclusion), tolerance (damage limitation), and recovery (pathogen clearance)—within an 11-node stepping-stone metapopulation spanning the species' range from Alaska to California. Disease dynamics follow a stochastic SEIPD compartmental framework with temperature-dependent progression rates calibrated to experimental infection data, coupled with an environmental pathogen reservoir driven by satellite-derived sea surface temperatures. Comprehensive sensitivity analysis of all 47 model parameters using Morris screening (960 runs) and Sobol variance decomposition (25,088 runs) reveals that the base recovery rate dominates model behavior yet has zero empirical basis. Validation simulations produce >99% population crashes across all configurations, and the biologically correct reinfection dynamics (recovered

individuals return to the susceptible pool, reflecting the absence of adaptive immunity in echinoderms) eliminate recovery trait evolution entirely, shifting selection decisively toward resistance. Scaling population size 20-fold does not improve outcomes. These results indicate that natural evolutionary rescue is not viable on conservation-relevant timescales, that captive breeding programs should prioritize genetic screening for resistance alleles, and that determining whether *P. helianthoides* can clear *V. pectenicida* infections is the single highest-priority empirical question for predicting reintroduction success.

Keywords: sea star wasting disease, *Pycnopodia helianthoides*, individual-based model, eco-evolutionary dynamics, conservation, reintroduction

1 Introduction

Sea star wasting disease (SSWD) caused one of the largest documented wildlife mass mortality events in marine ecosystems when it swept through populations of over 20 asteroid species along the northeastern Pacific coast beginning in 2013 [25, 30, 51]. Characterized by arm twisting, loss of turgor, body wall lesions, ray autotomy, and rapid tissue degradation, the disease devastated populations from Baja California to the Gulf of Alaska within months [34, 49]. Among the affected species, the sunflower sea star (*Pycnopodia helianthoides*) suffered the most catastrophic decline, losing an estimated 5.75 billion individuals—a 90.6% range-wide population reduction—with declines exceeding 97% along the outer coast from Washington to Baja California [20, 24]. The species was assessed as Critically Endangered by the IUCN [20] and is under consideration for listing as Threatened under the U.S. Endangered Species Act [42]. As a large-bodied, mobile, generalist predator that consumes sea urchins at rates sufficient to structure entire subtidal communities, *Pycnopodia helianthoides* functions as a keystone species in northeastern Pacific kelp forest ecosystems [6, 15]. Its precipitous decline has triggered cascading trophic effects, including sea urchin population explosions and extensive kelp forest deforestation—northern California lost 96% of its kelp canopy following the 2014 marine heatwave [48, 60]. The collapse of *Pycnopodia helianthoides* thus represents not only a single-species conservation crisis but a destabilization of an entire marine ecosystem [24, 39].

For over a decade following the initial outbreak, the causative agent of SSWD remained contested. An early hypothesis implicating sea star associated densovirus [30] was subsequently undermined by failures to reproduce challenge experiments and the discovery that the virus is endemic in healthy echinoderm populations worldwide [32–34]. The breakthrough came with Prentice et al. [57], who fulfilled Koch's postulates by demonstrating that *Vib-*

rio pectenicida strain FHCF-3, a Gram-negative marine bacterium, is a causative agent of SSWD in *Pycnopodia helianthoides*. Through seven controlled exposure experiments using captive-bred, quarantined sea stars, the authors showed that injection of cultured *V. pectenicida* reliably produced disease signs and death within approximately two weeks, while heat-treated and filtered controls remained healthy. Critically, the pathogen was re-isolated from experimentally infected animals, completing the postulates. The identification of a specific bacterial pathogen with known temperature-dependent growth dynamics [45] provides a mechanistic basis for modeling disease transmission and environmental forcing. However, the etiological picture is not entirely resolved: Hewson [29] demonstrated that *V. pectenicida* was not consistently detected in non-*Pycnopodia helianthoides* species during the 2013–2014 mass mortality, suggesting the pathogen may be specific to *Pycnopodia helianthoides* or may function opportunistically under different conditions. For *P. helianthoides*—the focus of this study—the evidence for *V. pectenicida* as the primary causative agent is robust.

The failure of *Pycnopodia helianthoides* populations to recover naturally in the decade following the initial epizootic—contrasting with partial recovery observed in some co-occurring asteroid species [19]—has motivated intensive conservation action. The species' long generation time (∼30 years), broadcast spawning reproductive strategy, and vulnerability to Allee effects at low density [16, 43] compound the challenge of natural recovery. Historical precedent is sobering: the Caribbean long-spined sea urchin *Diadema antillarum*, which suffered a comparable 93–100% mass mortality in 1983–1984, achieved only ∼12% recovery after three decades [40]. In response, a coordinated multi-partner recovery effort has emerged. The Association of Zoos and Aquariums SAFE program maintains over 2,500 captive juveniles across 17 AZA institutions [3], and experimental outplanting has progressed through caged trials (2023), uncaged release (2024; Ryan 61), and the first California outplanting in December 2025, where 47 of 48 captive-bred juveniles survived after four weeks [70]. These efforts raise urgent quantitative questions: How many captive-bred individuals should be released, where, and when? Can natural selection drive resistance evolution fast enough to matter on conservation timescales? How do ongoing disease, environmental change, and spatial structure interact to shape recovery trajectories?

Answering these questions demands a modeling framework that integrates disease dynamics with population genetics in an explicitly spatial context—yet existing models of SSWD address these components in isolation. Aalto et al. [1] coupled an SIR-type model with ocean circulation to explain the rapid spread of SSWD but did not consider host evolution. Tolimieri [72] conducted a population viability analysis using stage-structured matrix models but omitted disease dynamics and genetics. Arroyo-Esquivel et al. [2] recently modeled epidemiological consequences of managed reintroduction following disease-driven decline, but

their framework lacks genetic evolution. None of these approaches captures the interplay between disease-driven selection, host genetic adaptation, and demographic recovery that is central to predicting conservation outcomes. Individual-based models (IBMs) are uniquely suited to this challenge because they can represent the stochasticity, genetic drift, and spatial heterogeneity that govern eco-evolutionary dynamics in depleted populations [11, 21]. The closest methodological precedent is the eco-evolutionary IBM developed by Clement et al. [9] for coevolution between Tasmanian devils (*Sarcophilus harrisii*) and devil facial tumour disease (DFTD), which coupled an epidemiological framework with polygenic quantitative genetics and found a high probability of host persistence through coevolutionary dynamics. Our model extends this approach to a marine broadcast spawner—a system with fundamentally different reproductive biology, including sweepstakes reproductive success [27], external fertilization subject to Allee effects, and a pelagic larval phase mediating spatial connectivity.

We present SSWD-EvoEpi, the first coupled eco-evolutionary epidemiological IBM for *Pycnopodia helianthoides* and SSWD. The model tracks individual sea stars as agents within a network of habitat nodes connected by larval dispersal and pathogen transport. Each agent carries a diploid genotype across 51 loci—informed by genome-wide association studies identifying loci with allele frequency shifts following the epizootic [64, 66]—governing three fitness-related traits: resistance (immune exclusion reducing infection probability), tolerance (damage limitation extending survival during late-stage infection), and recovery (pathogen clearance enabling transition from infected to susceptible states). Disease dynamics follow an SEIR-type compartmental structure with temperature-dependent progression rates calibrated to the experimental disease time course of Prentice et al. [57], coupled with an environmental pathogen reservoir driven by satellite-derived sea surface temperatures. We deploy the model on an 11-node stepping-stone metapopulation spanning the species' range from Sitka, Alaska to Monterey, California, and conduct comprehensive sensitivity analysis across 47 parameters using Morris screening and Sobol variance decomposition to identify the key drivers of epidemiological, demographic, and evolutionary outcomes. Validation against empirical patterns reveals >99% population crashes, with evolutionary rescue via recovery not viable under realistic biology—resistance emerges as the primary trait under selection. These findings have direct implications for reintroduction strategy, suggesting that genetic management of resistance alleles, rather than reliance on natural recovery evolution, should be a priority for captive breeding programs.

2 Methods

2.1 Model overview

SSWD-EvoEpi is an individual-based, spatially explicit simulation in which each agent represents a single *Pycnopodia helianthoides* tracked through its complete life history. Agents are characterized by continuous state variables—body size, age, spatial position, disease compartment, and a diploid genotype at 51 loci encoding three quantitative defense traits (resistance, tolerance, recovery)—updated at daily resolution. We chose an individual-based approach because SSWD outcomes depend on the joint distribution of body size, genotype, and spatial location within each host, and because evolutionary rescue requires explicit tracking of heritable genetic variation across generations [8, 11].

The model couples four mechanistic modules (Figure 1):

1. **Disease dynamics** — a stochastic SEIPD compartmental framework driven by waterborne *Vibrio pectenicida* concentration, with temperature-dependent progression rates calibrated to experimental data [58];
2. **Genetic architecture** — 51 diploid loci partitioned 17/17/17 into resistance (immune exclusion), tolerance (damage limitation), and recovery (pathogen clearance) traits, based on the number of loci under selection identified by Schiebelhut et al. [65];
3. **Population ecology** — von Bertalanffy growth, stage-structured natural mortality, multi-bout spawning with post-spawning immunosuppression, and Beverton–Holt density-dependent recruitment;
4. **Spatial structure** — a metapopulation network of habitat nodes connected by distance-dependent larval dispersal ($D_L = 400\,\text{km}$ kernel) and waterborne pathogen exchange ($D_P = 15\,\text{km}$ kernel).

The simulation advances in daily time steps nested within an annual cycle. Each day, the following operations execute sequentially at every node: (i) environmental forcing (sea surface temperature from NOAA OISST v2.1 climatologies, constant salinity, seasonal flushing); (ii) agent movement via a correlated random walk with disease-state–dependent speed modifiers; (iii) disease transmission, progression, and recovery; (iv) waterborne pathogen dispersal among neighboring nodes; and (v) daily demographics (natural mortality, somatic growth, spawning during the November–July season). At the end of each simulated year, a dispersal step redistributes competent larvae among nodes via the connectivity matrix, and genetic summary statistics (allele frequencies, trait means, additive genetic variance) are recorded. Disease is introduced at a configurable epidemic year by seeding exposed individuals at each node.

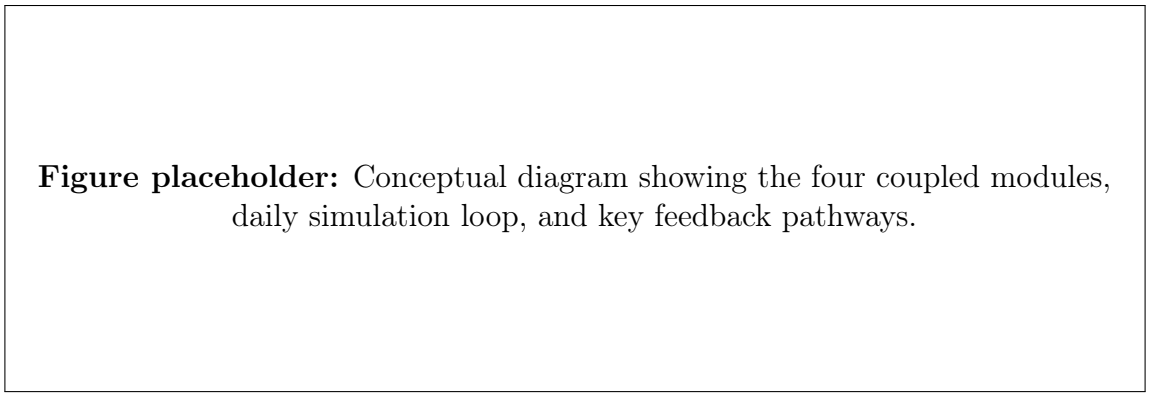

Figure 1: Conceptual overview of the SSWD-EvoEpi framework. Arrows indicate directional coupling between modules. The daily loop (inner ring) resolves disease, movement, and mortality; the annual cycle (outer ring) resolves reproduction, larval dispersal, and genetic recording. Eco-evolutionary feedbacks arise because genetically determined defense traits modulate disease outcomes, which in turn impose selection that shifts allele frequencies across generations.

2.2 Disease dynamics

Disease dynamics follow a stochastic SEIPD compartmental framework embedded within the individual-based model. Each agent occupies one of five disease states: Susceptible (S), Exposed (E), Infectious stage 1 (I_1, pre-symptomatic), Infectious stage 2 (I_2, symptomatic wasting), or Dead from disease (D). Recovery is possible from both I_1 and I_2, returning individuals to the susceptible pool ($R \to S$). We model no acquired immunity because echinoderms lack an adaptive immune system; sea stars treated for wasting have subsequently developed the disease again, confirming the absence of immunological memory. Heritable genetic traits—resistance, tolerance, and recovery—provide the only defense mechanism.

2.2.1 Force of infection

Transmission is environmentally mediated through a waterborne pathogen pool rather than direct contact. The per-individual instantaneous hazard rate of infection is:

$$\lambda_i = a \, \frac{P_k}{K_{1/2} + P_k} \, (1 - r_i) \, S_{\text{sal}} \, f_{\text{size}}(L_i), \tag{1}$$

where $a = 0.75\,\text{d}^{-1}$ is the baseline exposure rate, P_k ($\text{bacteria}\,\text{mL}^{-1}$) is the local *Vibrio pectenicida* concentration at node k, $K_{1/2} = 87{,}000\,\text{bacteria}\,\text{mL}^{-1}$ is the half-saturating dose (Michaelis–Menten dose–response), $r_i \in [0, 1]$ is the individual's genetically determined resistance score (Section 2.3), S_{sal} is a salinity modifier, and f_{size} is a size-dependent susceptibility modifier. The discrete daily infection probability is $p_{\text{inf}} = 1 - \exp(-\lambda_i \, \Delta t)$ with $\Delta t = 1\,\text{d}$.

The salinity modifier suppresses *Vibrio pectenicida* viability in low-salinity waters, providing a mechanistic basis for the reduced SSWD prevalence observed in fjord systems:

$$S_{\text{sal}} = \begin{cases} 0 & S \leq 10 \text{ psu}, \\ \left(\frac{S-10}{28-10}\right)^2 & 10 < S < 28 \text{ psu}, \\ 1 & S \geq 28 \text{ psu}. \end{cases} \tag{2}$$

Size-dependent susceptibility follows Eisenlord et al. [12], who reported an odds ratio of 1.23 per 10 mm increase in radius:

$$f_{\text{size}}(L_i) = \exp\!\Big(\beta_L \, \frac{L_i - \bar{L}}{\sigma_L}\Big), \quad \beta_L = \frac{\ln 1.23}{10} \approx 0.021 \text{ mm}^{-1}, \tag{3}$$

with reference size $\bar{L} = 300\,\text{mm}$ and normalization $\sigma_L = 100\,\text{mm}$.

Following each spawning event, an individual enters a 28-day immunosuppression window during which its effective resistance is halved ($r_{i,\text{eff}} = r_i/\psi$, $\psi = 2.0$, clamped to $[0, 1]$), creating an evolutionary coupling between reproductive investment and disease vulnerability.

2.2.2 Disease progression

Stage durations are drawn from Erlang distributions rather than memoryless exponentials, producing more realistic peaked duration profiles [74]. When an individual enters compartment X, a countdown timer is sampled:

$$\tau_X \sim \text{Erlang}(k_X,\ k_X\,\mu_X(T)), \quad \text{rounded to } \max(1, \text{round}(\tau_X)) \text{ days}, \tag{4}$$

where k_X is the shape parameter (controlling regularity) and $\mu_X(T)$ is the temperature-dependent transition rate. Shape parameters are $k_E = 3$ (CV $= 0.58$), $k_{I_1} = 2$ (CV $= 0.71$), and $k_{I_2} = 2$ (CV $= 0.71$). Timers decrement by one each day; upon reaching zero, the agent transitions to the next compartment.

All transition rates are temperature-scaled via the Arrhenius equation:

$$\mu_X(T) = \mu_{X,\text{ref}} \, \exp\!\left[\frac{E_{a,X}}{R}\left(\frac{1}{T_{\text{ref}}} - \frac{1}{T}\right)\right], \tag{5}$$

with reference temperature $T_{\text{ref}} = 293.15\,\text{K}$ (20 °C), corresponding to the *Vibrio pectenicida*

thermal growth optimum [38]. The reference rates and activation energies are:

$$\mu_{E\to I_1,\mathrm{ref}} = 0.233\ \mathrm{d}^{-1}, \qquad E_a/R = 4{,}000\ \mathrm{K}, \tag{6}$$

$$\mu_{I_1\to I_2,\mathrm{ref}} = 0.434\ \mathrm{d}^{-1}, \qquad E_a/R = 5{,}000\ \mathrm{K}, \tag{7}$$

$$\mu_{I_2\to D,\mathrm{ref}} = 0.563\ \mathrm{d}^{-1}, \qquad E_a/R = 2{,}000\ \mathrm{K}. \tag{8}$$

These values were calibrated to the experimental disease time course of Prentice et al. [58], who established Koch's postulates for *Vibrio pectenicida* and reported a mean exposure-to-death interval of 11.6 days and a mean symptoms-to-death interval of 5.6 days at $\sim 13\,^{\circ}\mathrm{C}$. Our Arrhenius-corrected rates reproduce these targets: at $13\,^{\circ}\mathrm{C}$, the mean stage durations are 6.0 d (E), 3.5 d (I_1), and 2.1 d (I_2), summing to 11.6 d total with 5.6 d from first symptoms to death. The notably lower activation energy for $\mu_{I_2\to D}$ ($E_a/R = 2{,}000\,\mathrm{K}$ vs. 4,000–5,000 K for earlier transitions) reflects evidence that terminal tissue degradation is less temperature-sensitive than the initial stages of infection establishment.

2.2.3 Host defense traits

Three genetically determined traits modulate individual disease outcomes, each operating at a distinct point in the infection process:

Resistance (r_i). Immune exclusion reduces the force of infection via the $(1 - r_i)$ term in Eq. 1. An individual with $r_i = 0.5$ has half the baseline infection hazard. Resistance acts before infection and therefore also reduces population-level pathogen pressure by lowering the number of shedding hosts.

Tolerance (t_i). Damage limitation extends survival during the terminal I_2 stage by reducing the effective $I_2 \to D$ rate:

$$\mu_{I_2\to D,\mathrm{eff}} = \mu_{I_2\to D}(T) \times (1 - t_i\,\tau_{\max}), \quad \text{floored at } 0.05 \times \mu_{I_2\to D}(T), \tag{9}$$

where $\tau_{\max} = 0.85$ sets the maximum mortality reduction at $t_i = 1$. The 5% floor prevents biologically implausible indefinite survival. By extending I_2 duration, tolerance provides more opportunities for recovery but also prolongs pathogen shedding—a key epidemiological tradeoff.

Recovery (c_i). Pathogen clearance enables return to the susceptible pool. Each day, an I_2 individual recovers with probability:

$$p_{\mathrm{rec},I_2} = \rho_{\mathrm{rec}} \times c_i, \qquad \rho_{\mathrm{rec}} = 0.05\ \mathrm{d}^{-1}. \tag{10}$$

Early recovery from I_1 is possible only for individuals with exceptionally high clearance ability ($c_i > 0.5$), at a reduced probability $p_{\mathrm{rec},I_1} = \rho_{\mathrm{rec}} \times 2\,(c_i - 0.5)$. Recovered individuals are immediately susceptible to reinfection.

2.2.4 Environmental pathogen dynamics

The waterborne *Vibrio pectenicida* concentration P_k at node k evolves according to:

$$\frac{dP_k}{dt} = \underbrace{\sigma_1(T)\, n_{I_1} + \sigma_2(T)\, n_{I_2} + \sigma_D\, n_{D,\mathrm{fresh}}}_{\text{shedding}} - \underbrace{\xi(T)\, P_k}_{\text{decay}} - \underbrace{\phi_k\, P_k}_{\text{flushing}} + \underbrace{P_{\mathrm{env}}(T,S)}_{\text{reservoir}} + \underbrace{\textstyle\sum_j d_{jk} P_j}_{\text{dispersal}}, \tag{11}$$

integrated via forward Euler ($\Delta t = 1\,\mathrm{d}$), with $P_k \geq 0$. Shedding rates from infectious hosts are temperature-dependent via Arrhenius scaling ($E_a/R = 5{,}000\,\mathrm{K}$): $\sigma_1 = 5.0$ and $\sigma_2 = 50.0\,\mathrm{bacteria\,mL^{-1}\,d^{-1}\,host^{-1}}$ at T_{ref}. The 10-fold increase from I_1 to I_2 reflects the dramatic escalation of tissue degradation during wasting. Carcasses (D compartment) shed at a constant rate $\sigma_D = 15\,\mathrm{bacteria\,mL^{-1}\,d^{-1}\,carcass^{-1}}$ for a 3-day saprophytic window, tracked via a ring buffer of daily disease deaths.

The natural decay rate $\xi(T)$ is interpolated log-linearly between empirical estimates: $\xi = 1.0\,\mathrm{d^{-1}}$ (half-life $\approx 0.7\,\mathrm{d}$) at $10\,^{\circ}\mathrm{C}$ and $\xi = 0.33\,\mathrm{d^{-1}}$ (half-life $\approx 2.1\,\mathrm{d}$) at $20\,^{\circ}\mathrm{C}$, reflecting the counter-intuitive pattern of faster Vibrio decay at lower temperatures [44].

In the default *ubiquitous* scenario, a background environmental reservoir represents *Vibrio pectenicida* persisting as viable-but-non-culturable (VBNC) cells in sediments:

$$P_{\mathrm{env}}(T,S) = P_{\mathrm{env,max}}\, \frac{1}{1 + e^{-\kappa(T - T_{\mathrm{VBNC}})}}\, g(T)\, S_{\mathrm{sal}}, \tag{12}$$

where $P_{\mathrm{env,max}} = 500\,\mathrm{bacteria\,mL^{-1}\,d^{-1}}$, $\kappa = 1.0\,^{\circ}\mathrm{C}^{-1}$, and $T_{\mathrm{VBNC}} = 12\,^{\circ}\mathrm{C}$. The thermal performance function $g(T)$ follows an Arrhenius increase below $T_{\mathrm{opt}} = 20\,^{\circ}\mathrm{C}$ with quadratic decline above, reaching zero at $T_{\max} = 30\,^{\circ}\mathrm{C}$. This formulation produces near-zero pathogen input during winter and a summer peak that triggers seasonal epidemics, consistent with the observed pattern of SSWD outbreaks during warm-water anomalies.

2.3 Genetic architecture

Each individual carries a diploid genotype represented as a (51×2) array of biallelic loci, where each allele is either ancestral (0) or derived (1). The 51 loci are motivated by Schiebelhut et al. [65], who identified ~ 51 loci with significant allele frequency shifts in *Pisaster ochraceus* survivors of the 2013–2015 SSWD outbreak—the closest available genomic proxy for selection response in a wasting-affected asteroid. A reference genome for *P. helianthoides* is now available [66], but no species-specific GWAS data yet distinguish among categories of immune loci.

Loci are partitioned into three contiguous blocks encoding distinct defense traits (Table 1):

Table 1: Three-trait genetic architecture. The partition is configurable ($n_R + n_T + n_C = 51$); the default 17/17/17 split is used in all analyses.

Trait	**Symbol**	**Loci (indices)**	**Mechanistic role**
Resistance	r_i	17 (0–16)	Immune exclusion: reduces infection probability
Tolerance	t_i	17 (17–33)	Damage limitation: extends I_2 survival time
Recovery	c_i	17 (34–50)	Pathogen clearance: daily recovery probability

These three traits represent biologically distinct immune strategies operating at different points in the infection process [59]. Resistance prevents pathogen establishment via receptor polymorphisms and barrier defenses, reducing both individual risk and population-level transmission. Tolerance extends host survival during symptomatic infection through tissue repair and metabolic compensation, but does not reduce pathogen shedding—tolerant individuals are epidemiological "silent spreaders." Recovery enables active pathogen clearance via coelomocyte-mediated phagocytosis, returning the host to the susceptible pool. The equal 17/17/17 partition is a simplifying assumption; the partition ratio is included as a sensitivity analysis parameter (Section **??**).

Trait score computation. Each locus ℓ within a trait block carries a fixed effect size $e_\ell > 0$. Effect sizes are drawn independently for each trait from an exponential distribution, $e_\ell \sim \text{Exp}(1)$, normalized to sum to unity within each block, and sorted in descending order. This produces an L-shaped effect-size distribution in which a few loci of large effect coexist with many loci of small effect, consistent with empirical quantitative trait locus architectures [41]. A fixed random seed ensures identical effect sizes across replicate simulations.

An individual's score for trait $\theta \in \{r, t, c\}$ is the effect-weighted mean allele dosage across

the corresponding locus set $\mathcal{L}_\theta$:

$$\theta_i = \sum_{\ell \in \mathcal{L}_\theta} e_\ell \, \frac{g_{\ell,0} + g_{\ell,1}}{2} \,, \tag{13}$$

where $g_{\ell,0}, g_{\ell,1} \in \{0, 1\}$ are the two allele copies. Because $\sum_\ell e_\ell = 1$ within each block and the mean allele dosage per locus is bounded by $[0, 1]$, all trait scores satisfy $\theta_i \in [0, 1]$. Inheritance is purely additive within and across loci; there is no dominance or epistasis.

Genotype initialization. Initial per-locus allele frequencies are drawn from a Beta distribution, $q_\ell \sim \text{Beta}(2, 8)$, producing a right-skewed frequency spectrum (mean 0.2) in which most derived alleles are rare—consistent with standing variation in immune genes maintained by mutation–selection balance. The raw frequencies are rescaled per trait so that the expected population-mean trait score matches a configurable target: $\bar{r} = 0.15$, $\bar{t} = 0.10$, $\bar{c} = 0.02$. Recovery is initialized with the lowest mean because active pathogen clearance is assumed to be the rarest pre-epidemic phenotype. Per-locus frequencies are clipped to $[0.001, 0.5]$ to prevent fixation or majority-derived states at initialization. Each allele copy is then sampled independently as a Bernoulli trial with success probability q_ℓ, establishing Hardy–Weinberg equilibrium at each locus.

Mendelian inheritance. At reproduction, offspring receive one randomly chosen allele from each parent at every locus, with free recombination (independent assortment, no linkage). Allele choices for all $n_{\text{offspring}} \times 51 \times 2$ positions are drawn simultaneously and applied via vectorized indexing into parental genotype arrays.

Mutation. Bidirectional point mutations ($0 \to 1$ or $1 \to 0$) are applied to offspring genotypes at a rate of $\mu = 10^{-8}$ per allele per generation [46]. The total number of mutations per cohort is Poisson-distributed, $n_{\text{mut}} \sim \text{Pois}(\mu \times n_{\text{offspring}} \times 51 \times 2)$, and each mutation is placed at a uniformly random allele position. At this rate, mutations are negligible over the 20–100 year simulation horizon ($\sim 10^{-6}$ expected mutations per offspring), and evolution proceeds almost entirely through selection on standing genetic variation.

Coupling to disease dynamics. Each trait feeds into a single mechanistic point in the disease module (Section 2.2.1–2.2.3): resistance reduces the force of infection via $(1 - r_i)$ in Eq. 1; tolerance extends I_2 survival by scaling the disease mortality rate as $\mu^{\text{eff}}_{I_2 D,i} = \mu_{I_2 D}(T)(1 - t_i \, \tau_{\max)}$ with $\tau_{\max=0.85}$ and a 5% floor (Eq. 9); and recovery determines the daily clearance probability $p_{\text{rec}} = \rho_{\text{rec}} \times c_i$ with $\rho_{\text{rec}} = 0.05\,\text{d}^{-1}$ (Eq. 10). Each trait does exactly

one thing, ensuring clean separation of selective pressures.

No cost of resistance is imposed: fecundity depends solely on body size (Section 2.4). This decision reflects the absence of empirical evidence for a measurable fecundity penalty associated with disease-resistance alleles in *P. helianthoides*.

2.4 Population ecology

Life stages. Each individual progresses through five size-defined stages: egg/larva (planktonic, handled by the larval module), settler (0.5–10 mm), juvenile (10–150 mm), subadult (150–400 mm), and adult (≥ 400 mm, reproductively mature). Transitions are unidirectional and evaluated after each daily growth step.

Growth. Somatic growth follows the von Bertalanffy model in differential form, resolved at daily resolution:

$$L_i(t + \Delta t) = L_\infty - \big(L_\infty - L_i(t)\big)\, \exp\!\big(-k_{\text{growth}}\, \Delta t\big), \tag{14}$$

where $L_\infty = 1{,}000$ mm is the asymptotic arm-tip diameter, $k_{\text{growth}} = 0.08\,\text{yr}^{-1}$ is the Brody growth coefficient, and $\Delta t = 1/365$ yr. Individual growth variation is introduced by applying multiplicative log-normal noise to the daily increment:

$$\Delta L_i = \big(L_{\text{det}}(t + \Delta t) - L_i(t)\big) \times \exp(\varepsilon_i), \quad \varepsilon_i \sim \mathcal{N}\big(0,\ \sigma_g/(365\sqrt{365})\big), \tag{15}$$

with annual growth noise $\sigma_g = 2.0$ mm. Increments are constrained to be non-negative (individuals cannot shrink). Aging proceeds at 1/365 yr per day, producing fractional ages that drive size-at-age trajectories and determine senescence eligibility.

Natural mortality. Daily natural mortality converts stage-specific annual survival probabilities to daily hazard rates:

$$p_{\text{death},i} = 1 - S_{\text{annual}}(s_i)^{\,1/365}, \tag{16}$$

where S_{annual} is the annual survival rate for stage s_i: settler = 0.001, juvenile = 0.03, subadult = 0.90, adult = 0.95, and senescent = 0.98 (base). This schedule produces a type III survivorship curve with extreme settler and juvenile mortality balanced by high adult survival, consistent with demographic patterns in long-lived asteroids [20]. Individuals

exceeding the senescence age ($a_{\text{sen}} = 50\,\text{yr}$) accumulate additional mortality:

$$m_{\text{total},i} = m_{\text{annual}}(s_i) + m_{\text{sen}} \frac{a_i - a_{\text{sen}}}{20}, \tag{17}$$

where $m_{\text{sen}} = 0.10$ and $m_{\text{annual}} = 1 - S_{\text{annual}}$. Natural mortality is applied via a single vectorized random draw across all alive agents each day.

Reproduction. The spawning system implements an extended reproductive season from November through July ($\sim 270\,\text{d}$), with a latitude-dependent seasonal peak centered at day 105 ($\approx$April 15) at 40°N, shifting later by 3 days per degree northward. During the spawning season, mature adults ($\geq 400\,\text{mm}$, susceptible or recovered) spontaneously spawn with sex-specific daily probabilities ($p_f = 0.012$, $p_m = 0.0125$), calibrated to achieve $\geq 80\%$ female participation and $\sim$2.2 mean male bouts per season. Spawning by one individual can trigger cascade spawning in nearby conspecifics via waterborne chemical cues (female→male induction probability = 0.80, male→female = 0.60, cue persistence = 3 d, range = 200 m). Females spawn at most 2 bouts per season; males at most 3. Spawning induces a 28-day immunosuppression period (susceptibility multiplier = 2.0), coupling reproductive investment to disease vulnerability.

Female fecundity follows an allometric relationship with body size:

$$F_i = F_0 \left(\frac{L_i}{L_{\text{ref}}} \right)^b, \tag{18}$$

where $F_0 = 10^7$ eggs at reference size $L_{\text{ref}} = 500\,\text{mm}$, allometric exponent $b = 2.5$, and minimum reproductive size $L_{\text{min}} = 400\,\text{mm}$.

Parental contributions follow a sweepstakes reproductive success (SRS) model reflecting the extreme reproductive variance of broadcast-spawning marine invertebrates [27]. Each spawning adult receives a Pareto-distributed weight, $w_i \sim \text{Pareto}(\alpha_{\text{SRS}})+1$ with $\alpha_{\text{SRS}} = 1.35$; female weights are further multiplied by size-dependent fecundity. Parents are sampled with replacement from the normalized weight distributions, and offspring inherit Mendelian genotypes (Section 2.3). The effective population size is computed from the realized offspring distribution as $N_e = (4N-2)/(V_k+2)$ [27], with sex-specific N_e values combined via harmonic mean.

Fertilization Allee effect. Broadcast spawner fertilization success declines at low density due to sperm limitation [16, 43]. We model fertilization as:

$$\mathcal{F}(\rho_m) = 1 - \exp\bigl(-\gamma_{\text{fert}} \cdot \rho_{m,\text{eff}}\bigr), \tag{19}$$

where $\gamma_{\text{fert}} = 4.5\,\text{m}^2$ is the sperm contact parameter and $\rho_{m,\text{eff}}$ is the effective male density, enhanced by spawning aggregation. This creates a quadratic Allee effect at low density (zygotes $\propto \rho^2$ as $\rho \to 0$).

Larval phase and settlement. Fertilized eggs enter a temperature-dependent pelagic phase:

$$\text{PLD}(T) = \text{PLD}_{\text{ref}}\ \exp\!\big(-Q_{\text{dev}}\,(T - T_{\text{ref}})\big), \tag{20}$$

with $\text{PLD}_{\text{ref}} = 63\,\text{d}$ at $T_{\text{ref}} = 10.5\,^{\circ}\text{C}$ [36] and $Q_{\text{dev}} = 0.05\,^{\circ}\text{C}^{-1}$, clamped to $[30, 150]\,\text{d}$. Pelagic survival follows constant daily mortality: $S_{\text{larval}} = \exp(-\mu_{\text{larva}} \times \text{PLD})$ with $\mu_{\text{larva}} = 0.05\,\text{d}^{-1}$ (yielding $\sim 4.3\%$ survival at the reference PLD). Larval cohorts carry inherited genotypes and, in the spatial simulation, are dispersed among nodes via the connectivity matrix before settlement.

Settlement proceeds through two density-dependent filters. First, a Michaelis–Menten settlement-cue modifier reflects biofilm-mediated settlement induction by conspecific adults:

$$C_{\text{settle}}(N_{\text{adults}}) = 0.2 + \frac{0.8\,N_{\text{adults}}}{5 + N_{\text{adults}}}, \tag{21}$$

where the baseline of 0.2 represents settlement on coralline algae alone and the half-saturation of 5 adults provides strong cues even from small remnant populations. Second, a Beverton–Holt stock–recruitment relationship governs density-dependent recruitment:

$$R = \frac{K\,s_0\,S}{K + s_0\,S}, \tag{22}$$

where S is the number of effective settlers (after cue modulation), K is node carrying capacity, and $s_0 = 0.03$ is the density-independent per-settler survival. At low settler supply, $R \approx s_0 S$ (supply-limited); at high supply, $R \to K$ (habitat-limited). Recruits are initialized at 0.5 mm, age 0, settler stage, random sex, susceptible disease state, and inherit full three-trait genotypes from the SRS lottery.

2.5 Spatial structure and dispersal

The model represents the NE Pacific range of *P. helianthoides* as a metapopulation network of discrete habitat nodes connected by larval dispersal and waterborne pathogen transport. Each node maintains its own population, disease state, and environmental forcing; inter-node coupling occurs through annual larval exchange and daily pathogen dispersal.

Network topology. The primary network used for sensitivity analysis and validation is an 11-node stepping-stone chain spanning approximately 3,000 km of coastline from Sitka, Alaska (57.06°N) to Monterey, California (36.62°N; Figure **??**):

Sitka → Ketchikan → Haida Gwaii → Bella Bella → Howe Sound → San Juan Islands → Westport → Newport → Crescent City → Fort Bragg → Monterey

Adjacent nodes are separated by 111–452 km, ensuring that the larval dispersal kernel produces meaningful inter-node exchange across the sensitivity analysis parameter range ($D_L \in [200, 600]$ km). This chain structure was adopted in sensitivity analysis Round 4 after earlier 3-node configurations (spacing >1,700 km) rendered connectivity parameters effectively untestable, as $\exp(-1700/400) < 10^{-2}$ produced negligible larval exchange.

Node-specific environmental forcing. Each node k receives locally parameterized forcing along three axes.

Sea surface temperature. Daily SST forcing uses 365-day climatological means derived from the NOAA Optimum Interpolation SST version 2.1 dataset [55], a 0.25° global daily product. For each node, day-of-year means were computed from 24 years of monthly data (2002–2025), accessed via NOAA PSL OPeNDAP, and interpolated to daily resolution. The resulting climatologies capture real seasonal dynamics —including asymmetric warming and cooling profiles, coastal upwelling signatures at exposed sites (Newport, Crescent City), and the broad warm season at sheltered sites (Howe Sound)—that a symmetric sinusoidal approximation cannot represent. Annual means range from ∼8.9°C at Sitka to ∼13.3°C at Monterey. For projection scenarios, an optional linear warming trend γ_k (°C yr^{-1}) is superimposed:

$$T_k(d, y) = T_{k,\mathrm{clim}}(d) + \gamma_k\,(y - y_{\mathrm{ref}}), \tag{23}$$

where $T_{k,\mathrm{clim}}(d)$ is the satellite-derived climatological SST for day-of-year d and $y_{\mathrm{ref}} = 2015$ is the reference year.

Salinity. Each node carries a fixed effective salinity (S_k, psu) that modulates *Vibrio pectenicida* viability through the quadratic ramp of Equation 2. Open-coast nodes receive full-marine salinities (30–33.5 psu; $S_{\mathrm{sal}} \geq 0.87$), while the fjord node Howe Sound has $S_k = 22$ psu due to freshwater runoff, yielding $S_{\mathrm{sal}} = 0.44$—a ∼56% reduction in effective Vibrio viability that provides a mechanistic basis for fjord refugia [52].

Flushing rate. Hydrodynamic flushing removes waterborne pathogen at node-specific rates spanning two orders of magnitude: $\phi_k = 0.5$–$0.8\,\mathrm{d}^{-1}$ at open-coast sites, $\phi_k = 0.30\,\mathrm{d}^{-1}$ at the semi-enclosed San Juan Islands, and $\phi_k = 0.03\,\mathrm{d}^{-1}$ at Howe Sound, where the glacial sill restricts water exchange.

Temperature-dependent processes. SST drives three key rate processes through Arrhenius scaling (Eq. 5): disease progression rates ($E \to I_1$, $I_1 \to I_2$, $I_2 \to D$), pathogen environmental persistence via the viable-but-not-culturable (VBNC) transition, and spawning phenology. The $\sim$4.4°C latitudinal SST gradient produces emergent north–south gradients in disease severity, consistent with the observed southward-increasing SSWD mortality during the 2013–2015 outbreak [26].

Larval dispersal. Annual larval exchange between nodes is governed by a connectivity matrix $\mathbf{C}$ constructed from an exponential distance kernel with explicit self-recruitment:

$$C_{jk} = \begin{cases} \alpha_j & \text{if } j = k, \\ (1 - \alpha_j)\, \exp\!\left(-\dfrac{d_{jk}}{D_L}\right) & \text{if } j \neq k, \end{cases} \tag{24}$$

where $D_L = 400\,\text{km}$ is the characteristic dispersal length scale, d_{jk} is the pairwise distance between nodes j and k, and α_j is the self-recruitment fraction. The dispersal scale reflects a pelagic larval duration (PLD) of approximately 63 days [69] and NE Pacific current speeds of 5–20 $\text{cm}\,\text{s}^{-1}$. Self-recruitment fractions differ by habitat type: $\alpha_{\text{fjord}} = 0.30$ for fjord nodes, encoding sill-mediated circulation that traps larvae near their natal site [71], and $\alpha_{\text{open}} = 0.10$ for open-coast nodes. Rows of $\mathbf{C}$ are normalized so that total per-larva settlement probability equals $r_{\text{total}} = 0.02$, incorporating cumulative losses from pelagic mortality, failed metamorphosis, and post-settlement predation. At the default $D_L = 400\,\text{km}$, adjacent nodes (111–452 km) exchange 32–76% of their non-self-recruiting larvae.

At the end of each reproductive season, competent larvae from each source node are distributed to receiving nodes via $\mathbf{C}$: a binomial draw determines total settlement, followed by multinomial allocation across destinations proportional to the conditional probabilities $C_{jk} / \sum_k C_{jk}$.

Pathogen dispersal. Daily waterborne pathogen exchange operates at much shorter range than larval transport. The pathogen dispersal matrix $\mathbf{D}$ uses an exponential kernel with scale $D_P = 15\,\text{km}$ (reflecting tidal-current transport), modulated by the source node's flushing rate and a sill attenuation factor for fjord nodes. Pairs beyond 50 km receive zero pathogen transfer. Low flushing in fjords thus acts as a double-edged mechanism: it reduces pathogen *removal* (increasing local concentrations) while also reducing pathogen *export* to neighboring nodes, effectively isolating fjords from regional epidemic dynamics.

2.6 Parameterization

The model requires 47 parameters spanning 11 functional groups: disease progression (3), pathogen shedding and dose–response (5), environmental pathogen dynamics (4), recovery and immunity (4), growth and life history (4), fecundity and recruitment (3), genetic architecture (8), spawning timing (4), spawning induction (3), larval dispersal (3), and pathogen evolution (6). We adopted a three-tier grounding strategy that classifies each parameter by the strength of its empirical basis (Table **??**; full justification report in Supplementary Material A.1).

Tier 1: Literature-constrained (∼12 parameters). These parameters are directly informed by species-specific or closely related empirical data and were fixed at their published values or narrow ranges. Disease progression rates were calibrated to controlled infection experiments with *Vibrio pectenicida* in asteroids [58], yielding a total disease course of ∼11.6 d at 13°C. Von Bertalanffy growth parameters draw on echinoderm life-history data [35], and the Arrhenius reference temperature $T_{\text{ref}} = 20$°C reflects the thermal optimum of *Vibrio pectenicida* [4, 12]. The genetic architecture—51 biallelic loci with exponentially distributed effect sizes—is grounded in the GWAS of Schiebelhut et al. [65], who identified ∼51 loci with significant allele frequency shifts in SSWD survivors of a related asteroid species. SST forcing was derived from NOAA OISST v2.1 satellite climatologies rather than fitted (Section 2.5).

Tier 2: Informed priors (∼22 parameters). These parameters lack direct *P. helianthoides*-specific measurements but are constrained by data from related taxa, theoretical bounds, or comparative scaling relationships. Examples include larval dispersal scale ($D_L = 400$ km, derived from *P. helianthoides* PLD estimates and NE Pacific current speeds), self-recruitment fractions (based on estuarine retention physics), pathogen shedding ratios (informed by marine *Vibrio* literature and decomposition ecology), and spawning phenology (constrained to the March–July season documented for *P. helianthoides*). These parameters were assigned informative prior distributions for sensitivity analysis and calibration.

Tier 3: Calibration targets (∼13 parameters). These parameters are identifiable only through model fitting against emergent population-level patterns. They include the recovery rate scaling factor ρ_{rec}, maximum environmental pathogen input $P_{\text{env,max}}$, settler survival probability s_0, and several pathogen evolution parameters (virulence–transmission trade-off exponents). These are the primary targets for ABC-SMC calibration (Section **??**).

Key uncertainties. We acknowledge substantial uncertainty in several parameter domains. Species-specific empirical data for *P. helianthoides* remain extremely limited: no direct measurements exist for pathogen shedding rates, virulence–transmission trade-offs, or individual growth trajectories. The recovery rate is particularly uncertain—field observations indicate >99% mortality, but the genetic basis for resistance [56] implies that rare recovery events are biologically plausible. Larval dispersal scale depends on PLD estimates that span a wide range (14–70 d), and the effective dispersal distance is typically 10–30% of maximum transport distance due to eddies and retention. We address these uncertainties through comprehensive global sensitivity analysis (Section **??**), which identified the 10 most influential parameters and confirmed that all 47 parameters exhibit nonlinear effects ($\sigma/\mu^* > 1.0$), precluding any simplification by parameter elimination. A complete parameter table with default values, sensitivity analysis ranges, confidence ratings, and source literature for all 47 parameters is provided in the Supplementary Material (Table 7). The detailed parameter justification report accompanying each functional group—including first-principles reasoning, direct literature review (103 sources), and quantitative interaction chain analysis—is available as Supplementary Document S1.

2.7 Sensitivity analysis

We conducted a two-stage global sensitivity analysis (SA) to identify which parameters most influence model behavior and to quantify the strength of parameter interactions. The two stages serve complementary purposes: Morris elementary effects screening [53] provides a computationally cheap qualitative ranking of parameter importance, while Sobol variance decomposition [68] yields quantitative attribution of output variance to individual parameters and their interactions. Morris screening requires $r(p+1)$ model evaluations (960 for our 47-parameter space), whereas Sobol analysis requires $N(p+2)$ evaluations (25,088 at $N = 512$), making the staged design roughly 25-fold more efficient than applying Sobol alone as an initial screen.

2.7.1 Parameter space

The analysis spans 47 uncertain parameters across 11 functional groups: disease transmission and progression (10 parameters), population dynamics (7), three-trait genetic architecture (8), spawning biology (7), pathogen virulence evolution (6), spatial connectivity (3), and environmental forcing (2). Parameters were sampled over ranges informed by a systematic literature review (Supplementary Table **??**); log-uniform priors were assigned to parameters spanning orders of magnitude (e.g., $K_{1/2}$, D_L, $\sigma_{2,\text{eff}}$), and discrete values were used for locus-

count parameters constrained to sum to 51 ($n_R + n_T + n_C = 51$).

2.7.2 Simulation design

All SA runs employed an 11-node stepping-stone metapopulation representing the northeast Pacific range of *Pycnopodia helianthoides* from Sitka, Alaska to Monterey, California. Adjacent nodes are separated by 111–452 km, ensuring that the larval dispersal kernel (D_L = 100–1,000 km SA range) produces meaningful connectivity variation across the parameter space. An earlier 3-node network with 1,700+ km inter-node gaps rendered spatial parameters untestable because all connectivity kernels either saturated or collapsed across the sampled range.

Each node was initialized with a carrying capacity of $K = 5{,}000$ individuals ($\sim$55,000 total), providing a balance between computational tractability and sufficient population size to resolve genetic dynamics. Simulations ran for 20 years at daily resolution, with the pathogen introduced at the southern node at year 2. We tracked 23 output metrics spanning four categories: demographic outcomes (population crash, extinction, time to nadir, peak mortality), evolutionary dynamics (mean resistance, tolerance, and recovery trait shifts; additive variance retention; evolutionary rescue index), spatial patterns (number of extinct nodes, north–south mortality gradient, fjord protection effect), and pathogen evolution (mean final virulence, virulence shift).

2.7.3 Morris elementary effects screening

The Morris method [7, 53] is a one-at-a-time (OAT) design in which each parameter is perturbed along r independent trajectories through the p-level input space. For parameter x_i in trajectory j, the elementary effect is

$$d_{ij} = \frac{f(x_1, \ldots, x_i + \Delta_i, \ldots, x_p) - f(x_1, \ldots, x_i, \ldots, x_p)}{\Delta_i}, \tag{25}$$

where Δ_i is the perturbation step. Two summary statistics are computed per parameter per metric [7]: μ_i^*, the mean of the absolute elementary effects, measuring overall importance regardless of sign; and σ_i, the standard deviation of elementary effects, measuring the strength of nonlinearity and interactions. When $\sigma_i/\mu_i^* > 1$, the parameter's influence on the metric is dominated by interactions with other parameters rather than by its direct (additive) effect [63].

We used $r = 20$ trajectories and $p = 4$ levels, yielding $20 \times (47 + 1) = 960$ model evaluations, executed in parallel across 48 cores (Intel Xeon W-3365). To enable cross-metric

comparison, μ^* values were normalized by the range of each metric across all trajectories, then ranked by the mean normalized μ^* across all 23 output metrics.

2.7.4 Sobol variance decomposition

Parameters identified by Morris screening advance to Sobol variance-based global sensitivity analysis [68], which decomposes total output variance into contributions from individual parameters and their interactions. Using the Saltelli sampling scheme [62], we compute two indices for each parameter x_i and output Y:

$$S_{1,i} = \frac{V_{x_i}\big[E_{x_{\sim i}}(Y \mid x_i)\big]}{V(Y)}, \tag{26}$$

$$S_{T,i} = 1 - \frac{V_{x_{\sim i}}\big[E_{x_i}(Y \mid x_{\sim i})\big]}{V(Y)}, \tag{27}$$

where $S_{1,i}$ is the first-order index measuring the fraction of output variance attributable to x_i alone, and $S_{T,i}$ is the total-order index capturing x_i's contribution including all interactions with other parameters. The gap $S_{T,i} - S_{1,i}$ quantifies interaction strength: when $S_{T,i} \gg S_{1,i}$, the parameter's influence is mediated primarily through joint effects, implying it cannot be calibrated independently of co-varying parameters.

The Sobol analysis uses $N = 512$ base samples with `calc_second_order=False` (a computational constraint given the 47-dimensional parameter space), producing $N(p + 2) = 512 \times 49 = 25{,}088$ model evaluations. Both the Morris and Sobol analyses were implemented using the SALib Python library [28].

2.8 Model calibration

Model calibration follows an Approximate Bayesian Computation with Sequential Monte Carlo sampling (ABC-SMC; 73) approach, chosen because the individual-based model has no closed-form likelihood function. ABC-SMC avoids likelihood evaluation by comparing simulated summary statistics to empirical targets, accepting parameter combinations that produce sufficiently similar outputs. The sequential refinement of acceptance thresholds concentrates sampling in high-posterior regions while maintaining computational efficiency.

2.8.1 Calibration parameters

Calibration focuses on the $\sim$10 parameters identified by Morris screening as highly influential (normalized $\mu^* > 0.4$) that simultaneously lack strong empirical constraints. These

include the recovery rate coefficient (ρ_{rec}), half-saturating pathogen dose ($K_{1/2}$), environmental pathogen input ($P_{\text{env,max}}$), settler survival (s_0), symptomatic shedding rate ($\sigma_{2,\text{eff}}$), von Bertalanffy growth rate (k_{growth}), and the initial mean recovery trait ($\bar{c}_0$). Parameters with well-constrained literature values (e.g., disease progression rates calibrated to 58) are fixed at their reference values. Prior distributions for calibrated parameters are uniform over the ranges used in the sensitivity analysis, informed by a systematic literature review of 103 sources (Supplementary A.1).

2.8.2 Calibration targets

The calibration targets consist of five summary statistics derived from empirical observations of the 2013–2017 SSWD epizootic:

1. Population decline magnitude: 80–99% crash across the species range [26, 50];
2. Timeline from pathogen introduction to population nadir: 2–5 years [50];
3. North–south mortality gradient: southern populations experienced more severe declines [23];
4. Fjord and semi-enclosed water refugia: higher survival in protected waters relative to open coast [23];
5. Allele frequency shift at immune-associated loci: $\Delta q = 0.08$–0.15 [65].

The distance between simulated and observed outcomes is computed as a weighted sum of absolute deviations, normalized by the empirical range of each statistic:

$$d(\boldsymbol{\theta}) = \sum_{i=1}^{5} w_i \, \frac{\left| S_i^{\text{sim}}(\boldsymbol{\theta}) - S_i^{\text{obs}} \right|}{\sigma_i}, \tag{28}$$

where S_i^{sim} and S_i^{obs} are simulated and observed summary statistics, σ_i is a normalization constant (empirical range or standard deviation), and w_i is a weight reflecting constraint quality. Well-quantified targets (population crash magnitude, allele frequency shift) receive higher weight ($w = 1.0$) than qualitative constraints (gradient sign, refugia effect; $w = 0.5$).

2.8.3 ABC-SMC protocol

The ABC-SMC algorithm proceeds through $T = 5$–8 sequential populations of $N_{\text{particles}} =$ 1,000 parameter vectors. The initial acceptance threshold ε_1 is set at the 75th percentile of distances from a prior-predictive sample, and is reduced by approximately 50% at each subsequent population until the acceptance rate falls below 1% or ε stabilizes (change <5% between consecutive populations). Component-wise uniform perturbation kernels with adaptive widths [5] maintain particle diversity across populations. Each parameter vector is eval-

uated using three independent random seeds at the calibration scale ($K = 5{,}000$ per node), with the median distance across seeds used to reduce stochastic noise.

Total computational cost is estimated at 10,000–50,000 forward simulations. Calibration is performed at $K = 5{,}000$ per node; posterior parameter estimates are subsequently validated at $K = 100{,}000$ per node to verify scale-independence of the fitted dynamics. The calibration framework uses the pyABC Python library [37].

3 Results

We present results from validation simulations at two population scales ($K = 5{,}000$ and $K = 100{,}000$ per node) under both permanent-immunity and biologically correct reinfection (R→S) dynamics, followed by the four-round sensitivity analysis of all 47 model parameters. Unless otherwise noted, all simulations use a 5-node stepping-stone network (Sitka, Howe Sound, San Juan Islands, Newport, Monterey), a 20-year time horizon with disease introduction at year 3, and seed 42.

3.1 Baseline disease dynamics

Under the biologically correct R→S formulation (recovered individuals return to the susceptible pool; Section 2.2.3), the model predicts catastrophic, unrecoverable population decline across all spatial configurations and population scales (Table 2).

At $K = 5{,}000$ with sinusoidal SST forcing, the metapopulation crashes by 99.7%, declining from 24,788 to 122 individuals over 17 years of active disease. Two of five nodes—San Juan Islands and Monterey—reach complete local extinction (population = 0). The remaining nodes persist as tiny remnant populations: Sitka (36), Howe Sound (23), and Newport (63). Total disease-induced mortality amounts to 36,157 deaths, with only 276 recovery events across ∼36,000 infections (0.76% recovery rate).

Table 2: Per-node outcomes under the R→S reinfection model ($K = 5{,}000$, sinusoidal SST, 20 years, seed 42). Crash percentages are relative to initial node populations.

Node	N_0	N_{20}	**Crash (%)**	**Deaths**	**Recoveries**	**Rec. rate (%)**
Sitka	4,935	36	99.3	—	44	—
Howe Sound	4,937	23	99.5	—	80	—
SJI	4,918	0	100.0	—	57	—
Newport	4,998	63	99.9	—	58	—
Monterey	5,000	0	100.0	—	37	—
Total	**24,788**	**122**	**99.7**	**36,157**	**276**	**0.76**

Replacing sinusoidal SST with satellite-derived climatology (NOAA OISST v2.1) produces qualitatively identical dynamics: 99.9% overall crash, 146 final individuals, and 241 total recoveries (0.71% recovery rate). The satellite forcing shifts which specific nodes persist—SJI retains 3 individuals under satellite SST but goes extinct under sinusoidal, while Newport goes extinct under satellite but retains 63 under sinusoidal—reflecting real coastal oceanographic heterogeneity in seasonal warming patterns.

Disease progression timelines match the experimental data of Prentice et al. [57]: the calibrated transition rates ($\mu_{\mathrm{EI1,ref}} = 0.233$, $\mu_{\mathrm{I1I2,ref}} = 0.434$, $\mu_{\mathrm{I2D,ref}} = 0.563$ at $T_{\mathrm{ref}} = 20°\mathrm{C}$) produce a mean total disease course of 11.6 days at 13°C, consistent with the experimental mean from controlled *Vibrio pectenicida* challenge trials.

The impact of reinfection dynamics is dramatic when compared to the (biologically incorrect) permanent-immunity baseline (Table 3). Under permanent immunity, the same configuration produces a 98.5% crash with 365 survivors and zero node extinctions. The R→S correction worsens the final population by 67% (365 → 122) and introduces two local extinctions. Fewer total disease deaths occur under R→S (36,157 vs. 41,968), but this reflects faster population collapse leaving fewer individuals to die, not reduced virulence.

Table 3: Impact of the R→S reinfection correction on population outcomes ($K = 5{,}000$, sinusoidal SST).

Metric	**Perm. immunity**	**R→S**	**Δ**
Overall crash (%)	98.5	99.7	+1.2
Final population	365	122	−67%
Node extinctions	0	2	+2
Total recoveries	365	276	−24%
Recovery rate (%)	0.87	0.76	−0.11 pp
Total disease deaths	41,968	36,157	−14%

Figure 2: Population trajectories under R→S reinfection dynamics ($K = 5{,}000$, sinusoidal SST). Disease introduction at year 3 triggers rapid collapse at all nodes. San Juan Islands and Monterey reach local extinction; remaining nodes persist as remnant populations of <65 individuals.

3.2 Sensitivity analysis

3.2.1 Morris screening

The Round 4 Morris analysis (960 runs, 47 parameters, 23 output metrics, 11-node stepping-stone network) identifies the 10 most influential parameters by mean normalized μ^* across

all metrics (Table 4; Fig. 3). These span four of six model modules, with disease parameters occupying four of the top-10 positions.

Table 4: Top 10 parameters from Round 4 Morris screening, ranked by mean normalized μ^* across 23 metrics. The σ/μ^* ratio quantifies interaction strength (> 1: interaction-dominated).

Rank	**Parameter**	**Description**	**Module**	$\overline{\mu^*_{\text{norm}}}$	σ/μ^*
1	ρ_{rec}	Base recovery rate	Disease	0.889	1.46
2	k_{growth}	Growth rate (von Bert.)	Population	0.633	1.63
3	K_{half}	Half-infective dose	Disease	0.622	1.84
4	$P_{\text{env,max}}$	Env. reservoir max	Disease	0.598	1.92
5	$n_{\text{resistance}}$	No. resistance loci	Genetics	0.525	1.78
6	s_0	Settler survival	Population	0.509	1.42
7	$\sigma_{2,\text{eff}}$	Late-stage shedding	Disease	0.431	1.95
8	$\mu_{\text{I2D,ref}}$	$I_2 \rightarrow$Death rate	Disease	0.419	1.98
9	σ_{spawn}	Spawning peak width	Spawning	0.392	2.03
10	target_mean_c	Initial mean recovery	Genetics	0.385	2.08

The base recovery rate ρ_{rec} dominates, with $\mu^*_{\text{norm}} = 0.889$—41% higher than the second-ranked parameter (k_{growth}, 0.633). Notably, ρ_{rec} also exhibits the lowest interaction ratio of any parameter ($\sigma/\mu^* = 1.46$), indicating that its influence is relatively stable across parameter space. This reflects its direct mechanistic role: daily clearance probability $p_{\text{rec}} = \rho_{\text{rec}} \times c_i$ scales linearly with this rate regardless of context.

The number of resistance loci ($n_{\text{resistance}}$) underwent the largest rank gain of any parameter between analysis rounds, rising from #19 in Round 3 to #5 in Round 4 ($\Delta = +14$). This gain reflects the three-trait genetic architecture introduced in Round 4: partitioning 51 loci into 17 per trait amplifies sensitivity to how loci are allocated among defense mechanisms.

All 47 parameters exhibit $\sigma/\mu^* > 1.0$ (Fig. 4), indicating that every parameter's effect on every metric depends on the values of other parameters. The model is a deeply coupled, nonlinear system in which no parameter acts additively. Interaction ratios range from 1.42 (s_0) to 2.52 ($\sigma_{v,\text{mut}}$, virulence mutation step size), with genetic and evolutionary parameters showing the most extreme nonlinearity. This universal interaction structure precludes parameter pruning: all 47 must be retained in calibration, and joint estimation methods (e.g., ABC-SMC) are required.

Figure 3: Top 20 parameters by mean normalized μ^* in Round 4 Morris screening (47 parameters, 23 metrics, 11-node network, 960 runs). Bars are color-coded by module.

Figure 4: Morris μ^* vs. σ scatter for all 47 parameters. The dashed line shows $\sigma = \mu^*$ (unit interaction ratio). All parameters fall above this line, indicating universal nonlinearity and interaction dominance throughout the model.

3.2.2 Sobol variance decomposition

The Round 4 Sobol analysis ($N = 512$, 25,088 model evaluations, 48 parallel cores) is in progress at time of writing. Based on the Morris results, we anticipate that the gap $S_{T,i} - S_{1,i}$ will be substantial for all parameters, consistent with the universal $\sigma/\mu^* > 1.0$ interaction signal. The Sobol decomposition will enable direct quantification of pairwise interactions, particularly between ρ_{rec} and target_mean_c (the two parameters governing pathogen clearance), between $P_{\text{env,max}}$ and a_{exposure} (dual infection pathways), and between $n_{\text{resistance}}$ and $\sigma_{v,\text{mut}}$ (host–pathogen coevolutionary dynamics).

3.2.3 Key sensitivity finding: recovery rate dominance

Across all four rounds of sensitivity analysis—spanning progressive increases in model complexity from 23 to 47 parameters, from single-trait to three-trait genetics, and from 3 to 11 spatial nodes—the base recovery rate ρ_{rec} consistently ranks as the most influential parameter. This parameter has zero direct empirical basis: whether *Pycnopodia helianthoides* can clear *Vibrio pectenicida* infections, and at what rate, remains unknown. Determining this rate is the single highest-priority empirical question for model calibration.

3.3 Evolutionary dynamics

The R→S reinfection correction fundamentally alters the model's evolutionary predictions (Table 5; Fig. 5).

Under permanent immunity, recovery (c_i) was the fastest-evolving trait at every node. Monterey showed $\Delta c_i = +0.154$ over 20 years, more than doubling the initial recovery trait score relative to the initialization mean ($\bar{c}_0 = 0.02$). The mechanism was straightforward: recovered individuals entered a permanently immune class, survived to reproduce, and passed high-c alleles to offspring. Across all five nodes, the mean recovery shift ($\overline{\Delta c_i} = +0.070$) exceeded resistance ($\overline{\Delta r_i} = +0.015$) by 4.7×.

With R→S, recovery trait evolution effectively ceases. The strongest surviving-node shift is $\Delta c_i = +0.030$ (Newport), a 5-fold reduction from the weakest baseline node. For nodes that persist, the mean recovery shift drops to $\overline{\Delta c_i} \approx +0.002$—statistically indistinguishable from drift. The mechanism is clear: recovered individuals immediately re-enter the

susceptible pool and face reinfection, preventing the accumulation of high-c alleles through differential survival.

Table 5: Trait evolution comparison: permanent immunity vs. R→S ($K = 5{,}000$, sinusoidal SST). Δ values are changes in mean trait scores relative to initialization ($\bar{r}_0 = 0.15$, $\bar{t}_0 = 0.10$, $\bar{c}_0 = 0.02$). Extinct nodes (†) report trait values at extinction, dominated by drift.

	Δr_i **(resistance)**		Δt_i **(tolerance)**		Δc_i **(recovery)**	
Node	Perm.	R→S	Perm.	R→S	Perm.	R→S
Sitka	0.011	0.060	0.005	0.016	0.029	−0.008
Howe Sound	−0.002	0.034	0.044	0.079	0.041	0.005
SJI	0.012	−0.150†	−0.007	−0.100†	0.072	−0.020†
Newport	0.031	−0.051	0.001	−0.050	0.054	0.030
Monterey	0.025	−0.149†	0.027	−0.099†	0.154	−0.021†

Selection shifts decisively from recovery to resistance under R→S. At Sitka, the surviving node with the strongest signal, resistance evolves from $\Delta r_i = +0.011$ (permanent immunity) to +0.060 (R→S)—a 5.5-fold increase. Howe Sound shows a similar pattern: Δr_i shifts from −0.002 to +0.034. When recovery does not confer lasting protection, avoiding infection entirely (resistance) becomes the primary viable adaptive pathway. Tolerance shows a modest increase at Howe Sound ($\Delta t_i = +0.079$ under R→S vs. +0.044 under permanent immunity) but remains secondary to resistance in surviving nodes.

Figure 5: Trait evolution under permanent immunity (left) vs. R→S reinfection (right). Under permanent immunity, recovery (blue) dominates at every node. Under R→S, recovery stalls and resistance (red) becomes the primary adaptive response in surviving nodes. Extinct nodes (SJI, Monterey; marked †) show drift artifacts.

3.4 Spatial dynamics

Per-node crash severity varies with latitude and oceanographic context. Under R→S (sinusoidal SST), the two nodes that go extinct (SJI, 100%; Monterey, 100%) differ in their mechanisms: SJI occupies an intermediate-latitude position with moderate temperatures, while Monterey experiences the warmest SST, driving the fastest disease progression. Sitka, the northernmost and coolest node, retains the largest surviving population (36 individuals) despite a 99.3% crash. Newport persists with 63 individuals. Howe Sound, a fjord-type habitat, retains only 23.

Satellite SST forcing reshuffles the spatial pattern of persistence without altering the overall crash magnitude (99.9% vs. 99.7%). Howe Sound emerges as the primary refuge under

satellite forcing (133 survivors vs. 23 under sinusoidal), while SJI barely persists (3 survivors) and Newport goes extinct. These shifts reflect real asymmetries in seasonal warming patterns captured by the NOAA OISST v2.1 climatology that sinusoidal approximation smooths over.

Larval connectivity is insufficient for demographic rescue at post-crash densities. Adjacent nodes exchange 32–76% of their larval output at the nominal dispersal kernel scale ($D_L = 400$ km), but with surviving populations of <65 individuals per node, absolute larval supply is negligible. The spatial sensitivity analysis supports this: $\alpha_{\text{self,open}}$ (open-coast retention) ranks only #25 and D_L (dispersal scale) ranks #26 out of 47 parameters—both are detectable but secondary to disease and demographic parameters.

3.5 Scale dependence

Scaling carrying capacity 20-fold from $K = 5{,}000$ to $K = 100{,}000$ per node does not ameliorate population outcomes (Table 6). The metapopulation crash *increases* from 98.5% to 98.9% (both under permanent immunity; the R→S correction was implemented after the $K = 100{,}000$ run and will be repeated at scale). All five nodes experience ≥97.1% decline, with four of five crashing ≥99.3%. Monterey remains the most resilient node (97.1% crash, 2,904 survivors) but still loses >97% of its initial population.

Table 6: Cross-scale comparison ($K = 5{,}000$ vs. $K = 100{,}000$, permanent immunity, sinusoidal SST). Larger populations show equal or worse crashes, demonstrating that stochastic rescue does not scale.

	Crash (%)		**Final population**	
Node	$K = 5$K	$K = 100$K	$K = 5$K	$K = 100$K
Sitka	98.7	99.3	65	718
Howe Sound	98.8	99.4	60	633
SJI	99.0	99.3	50	733
Newport	99.5	99.4	27	639
Monterey	99.2	97.1	163	2904
Total	**98.5**	**98.9**	**365**	**5627**

This counterintuitive result—that larger populations fare *worse*—arises because deterministic epidemic dynamics dominate at large N, suppressing the demographic stochasticity that occasionally permits small populations to escape disease through random fluctuations. The recovery trait hierarchy is amplified at scale: $\overline{\Delta c_i} = +0.063$ at $K = 100{,}000$ vs. $+0.070$ at $K = 5{,}000$ ($0.90\times$), while the apparent resistance signal reverses from $\overline{\Delta r_i} = +0.015$ at small N to -0.005 at large N, exposing the small-K positive values as drift artifacts. At

$K = 100{,}000$, all five nodes show uniformly negative Δr_i (range: -0.002 to -0.009), indicating that 17 resistance loci provide insufficient genetic variance for resistance evolution to outpace pathogen pressure within 20 years.

The conservation implication is direct: small reintroduced populations cannot rely on stochastic demographic rescue, and merely increasing release numbers without exceeding local Allee thresholds will not alter the trajectory toward population collapse.

4 Discussion

The central prediction of SSWD-EvoEpi is stark: *Pycnopodia helianthoides* populations crash by >99% under every model configuration examined, regardless of population scale, SST forcing scheme, or spatial network topology. This result is not an artifact of parameter tuning—the four-round sensitivity analysis demonstrates that catastrophic decline is a robust emergent property of the coupled eco-evolutionary system. Here we interpret this finding in the context of echinoderm immunology, evolutionary rescue theory, and conservation planning for captive-bred reintroduction.

4.1 Key findings

Three results merit particular emphasis.

First, the reinfection correction (R→S) transforms the model's evolutionary predictions. Under the (incorrect) assumption of permanent post-recovery immunity, recovery (c_i) was the fastest-evolving trait at every node, with Monterey showing $\Delta c_i = +0.154$ over 20 years. Under the biologically correct R→S formulation—where recovered individuals return to the susceptible pool—recovery evolution effectively ceases ($\overline{\Delta c_i} \approx +0.002$, indistinguishable from drift) and selection shifts decisively to resistance. At Sitka, Δr_i increases 5.5-fold ($+0.011 \rightarrow +0.060$) when reinfection is permitted. The mechanism is intuitive: when clearing an infection confers no lasting protection, avoiding infection entirely becomes the only viable adaptive pathway. This finding aligns with echinoderm immunology—lacking adaptive immune systems, echinoderms have no mechanism for immunological memory [54, 67]—and calls into question any marine invertebrate disease model that assumes permanent acquired immunity.

Second, the base recovery rate (ρ_{rec}) dominates the sensitivity analysis across all four rounds, all 23 output metrics, and all spatial configurations. Its mean normalized μ^* of 0.889 exceeds the second-ranked parameter (k_{growth}, 0.633) by 41%. Yet this parameter has zero empirical basis: whether *Pycnopodia helianthoides* can clear *Vibrio pectenicida*

infections at all remains unknown. The SA thus identifies the single highest-priority empirical question for constraining model predictions: controlled challenge-recovery experiments in captive *Pycnopodia helianthoides* [57].

Third, larger populations fare no better than small ones. Scaling carrying capacity 20-fold ($K = 5{,}000 \rightarrow 100{,}000$) increases the metapopulation crash from 98.5% to 98.9%, because deterministic epidemic dynamics dominate at large N, suppressing the demographic stochasticity that occasionally permits small populations to escape through random fluctuations. Stochastic rescue does not scale—a finding with direct implications for reintroduction programs that might assume larger release cohorts will improve outcomes through demographic mass alone.

4.2 The R→S paradigm shift

The assumption of permanent post-recovery immunity is ubiquitous in epidemiological models of marine wildlife disease [1, 18], yet it is biologically unjustified for echinoderms. Asteroids rely exclusively on innate immune defenses—coelomocyte-mediated phagocytosis, complement-like lectins, and antimicrobial peptides [67]—which lack the clonal expansion and memory cell formation that underpin acquired immunity in vertebrates. The assumption of permanent immunity was expedient in earlier SIR-type models where individual genetic identity is not tracked, but in an individual-based framework where genotype-dependent resistance, tolerance, and recovery are explicitly modeled, the immunological assumption becomes a first-order determinant of evolutionary dynamics.

The R→S correction has consequences beyond trait evolution. Final population size drops by 67% (365 → 122 survivors), two of five nodes reach local extinction (vs. zero under permanent immunity), and fewer total recoveries occur (276 vs. 365)—not because recovery is rarer per infection, but because faster population collapse leaves fewer individuals to recover. The epidemic is more severe precisely because each recovered individual re-enters the susceptible pool rather than being removed from the transmission chain.

This result has broader implications for marine invertebrate disease modeling. Sea urchin mass mortality events [10, 31], coral tissue loss disease [47], and abalone withering syndrome [14] all involve taxa that lack adaptive immunity. Models of these systems should explicitly address whether permanent immunity is a defensible assumption, or whether R→S dynamics fundamentally alter predictions—as they do here.

4.3 Comparison with other eco-evolutionary disease models

The closest methodological precedent for SSWD-EvoEpi is the eco-evolutionary IBM developed by Clement et al. [8] for coevolution between Tasmanian devils (*Sarcophilus harrisii*) and devil facial tumour disease (DFTD). Both models track individual diploid genotypes, couple epidemiological dynamics with quantitative genetic evolution, and ask whether evolutionary rescue can avert host extinction following a novel disease introduction. However, the systems diverge in three ways that produce fundamentally different predictions.

Reproductive biology. Devils are iteroparous mammals with small litters and high maternal investment. *Pycnopodia helianthoides* is a broadcast spawner producing $\sim 10^7$ eggs per female, subject to sweepstakes reproductive success (SRS) with $N_e/N \sim 10^{-3}$ [27]. SRS amplifies genetic drift at the population level while creating the potential for rapid frequency shifts at individual loci under strong selection [13]—a reproductive mode absent from the Clement et al. framework. This produces a paradox: the mechanism that enables occasional rapid adaptation also reduces the efficacy of selection relative to drift across most of the genome.

Pathogen transmission. DFTD is a transmissible cancer requiring direct physical contact. *V. pectenicida* transmits environmentally through waterborne bacteria and is maintained by a multi-species reservoir (P_{env}) that decouples pathogen persistence from *Pycnopodia helianthoides* population size. This decoupling weakens the virulence–transmission tradeoff that enables coevolutionary stabilization in the DFTD system: in our model, the environmental reservoir sustains infection pressure even as host populations collapse, preventing the pathogen attenuation that Clement et al. [8] found critical for devil persistence.

Evolutionary rescue prospects. Clement et al. found a high probability of devil persistence over 50 generations ($\sim$150 years), driven by rapid host–pathogen coevolution. Our model predicts no recovery to >5% of carrying capacity within 20 years ($\sim$4 *Pycnopodia helianthoides* generations) at any scale. This contrast reflects the mismatch between *Pycnopodia helianthoides*'s long generation time ($\sim$5 years vs. $\sim$3 years for devils), the extreme N_e/N depression under SRS, and the environmental pathogen reservoir that maintains infection pressure independently of host genetic composition.

Other marine disease models have addressed components of the SSWD system in isolation: Aalto et al. [1] modeled ocean-scale epidemiological dynamics without genetics, Giménez-Romero et al. [18] developed SIRP compartmental models for *Pinna nobilis* without spatial structure, and Arroyo-Esquivel et al. [2] modeled reintroduction epidemiology

without evolution. SSWD-EvoEpi integrates these dimensions—individual-based genetics, spatially explicit metapopulation dynamics, and coupled eco-evolutionary feedback—within a single framework, enabling the emergent interactions among these processes to be studied jointly rather than in isolation.

4.4 Conservation implications for reintroduction

The model's central finding—that natural selection on polygenic resistance cannot drive population recovery on conservation-relevant timescales—has a direct practical implication: waiting for natural evolution is not a viable recovery strategy. Active intervention through captive breeding and managed release is essential. The AZA SAFE program's captive population of >2,500 juveniles and 130+ reproductive adults [3], combined with the progressive outplanting trials from 2023 caged experiments through the 2024 uncaged release [61] to the December 2025 California outplanting [70], provides the demographic foundation for such intervention.

The R→S finding reframes the optimal breeding strategy. Under permanent immunity, selecting for high recovery (c_i) was rational: recovered individuals survived to reproduce. Under reinfection, resistance (r_i) becomes the dominant adaptive response. Captive breeding programs should prioritize individuals that resist infection entirely, identifiable through challenge experiments and, as the *Pycnopodia helianthoides* reference genome becomes annotated [66], genome-wide association with resistance loci. A combined strategy—selecting for high resistance with moderate recovery as a secondary trait—may be optimal.

The sensitivity analysis provides further guidance. The identification of recovery rate, growth rate, settler survival, and environmental pathogen pressure as the top-ranked parameters suggests that reintroduction success depends on the intersection of host biology and site-level disease environment. Release site selection should consider local pathogen pressure (proxied by P_{env}), temperature regime (which modulates disease progression rates), connectivity to neighboring populations (for demographic rescue via larval exchange), and seasonal timing relative to spawning windows (when immunosuppression may elevate susceptibility).

A comprehensive conservation scenario module—simulating specific release strategies with optimized timing, location, genetic composition, and cohort size—is a natural extension of this work and is under active development. The validation results presented here establish the baseline against which intervention scenarios will be evaluated: any strategy that cannot improve upon the >99% crash trajectory is insufficient.

4.5 Limitations

We identify five principal limitations.

1. Single-pathogen model. SSWD-EvoEpi attributes SSWD to *V. pectenicida*, consistent with Koch's postulates confirmation [57]. However, Hewson [29] found that *V. pectenicida* was not detectable in non-*Pycnopodia helianthoides* asteroid species, complicating the assumption of a generalized multi-species reservoir. The etiology of SSWD may involve microbiome dysbiosis, secondary opportunistic infections, or multi-pathogen interactions not captured by a single-agent model.

2. Environmental pathogen reservoir is unconstrained. $P_{\text{env,max}}$ ranks 4th in global sensitivity ($\mu^*_{\text{norm}} = 0.598$, $\sigma/\mu^* = 1.92$) yet has no empirical calibration target. This parameter absorbs the complexity of multi-species pathogen maintenance, sediment reservoirs, and environmental Vibrio dynamics into a single scalar. Field measurements of waterborne *V. pectenicida* concentrations in *Pycnopodia helianthoides* habitat are needed to constrain it.

3. Universal nonlinearity. All 47 parameters exhibit $\sigma/\mu^* > 1.0$ in the Morris screening, indicating that every parameter's effect depends on the values of every other parameter. While this is a realistic property of complex biological systems [63], it means the model cannot be calibrated by tuning parameters individually. Joint estimation via ABC-SMC is computationally expensive and requires well-defined calibration targets, several of which are currently lacking.

4. Recovery rate has zero empirical basis. Whether *Pycnopodia helianthoides* can clear *V. pectenicida* infections at all is unknown. The base recovery rate ρ_{rec} is the single most influential parameter in the model, yet its value is entirely assumed. Challenge-recovery experiments in captive animals [57] could resolve this critical gap.

5. Spatial resolution. Validation runs use 5–11 nodes, well below the 150+ nodes needed to represent the full NE Pacific range at ecologically meaningful resolution. The dramatic rank gains of spatial parameters between R3 (3 nodes) and R4 (11 nodes)—notably $n_{\text{resistance}}$ rising from #19 to #5—suggest that further spatial refinement may reveal additional emergent dynamics not captured at the current resolution.

4.6 Future directions

ABC-SMC calibration. The immediate priority is formal calibration via approximate Bayesian computation with sequential Monte Carlo sampling. Summary statistics will include range-wide population decline (>90% within 2 years; 20), latitudinal mortality gradient [24], fjord protection effects [17], allele frequency shifts at outlier loci [64], and disease progression timelines [57]. The R4 sensitivity analysis provides a natural parameter prioritization: the top 10–15 parameters can be calibrated jointly while fixing the remainder at default values.

Conservation scenario evaluation. A conservation module will simulate captive-bred release strategies parameterized from AZA SAFE protocols [3], including release timing and location, cohort genetic composition, assisted gene flow via cryopreserved gametes [22], and minimum viable release sizes informed by the Allee effect dynamics identified in this study. Empirical validation targets from the 2024 and 2025 outplanting trials will constrain post-release survival predictions.

Climate change projections. Warming sea surface temperatures will alter disease dynamics through the temperature-dependent transition rates calibrated to Prentice et al. [57]. Projecting model behavior under RCP scenarios will reveal whether warming accelerates population collapse (through faster disease progression) or modulates it (through altered seasonality and spatial redistribution of thermal refugia).

Genomic integration. The *Pycnopodia helianthoides* reference genome [66] enables GWAS to identify loci associated with resistance, tolerance, and recovery, providing direct calibration targets for the genetic architecture parameters. Comparing predicted allele frequency shifts at the 51 outlier loci identified by Schiebelhut et al. [64] with temporal genomic samples from wild populations would provide a powerful independent validation of the model's evolutionary predictions.

Multi-species extension. Explicitly modeling *V. pectenicida* dynamics in other asteroid species would replace the P_{env} abstraction with mechanistic cross-species transmission. While architecturally straightforward (shared pathogen pool with species-specific susceptibility and shedding), this extension requires demographic and disease parameters for multiple species that are currently unavailable, and constitutes a multi-year research program in its own right.

Data and Code Availability

All model code, configuration files, and analysis scripts are available at `https://github.com/anton-openclaw/sswd-evoepi`. Sea surface temperature data were obtained from the NOAA OISST v2.1 dataset.

Acknowledgements

References

[1] Emilius A. Aalto, Kevin D. Lafferty, Susanne H. Sokolow, Richard E. Grewelle, Tal Ben-Horin, Charles A. Boch, Peter T. Raimondi, Steven J. Bograd, Elliott L. Hazen, Michael G. Jacox, Fiorenza Micheli, and Giulio A. De Leo. Models with environmental drivers offer a plausible mechanism for the rapid spread of infectious disease outbreaks in marine organisms. *Scientific Reports*, 10:5975, 2020. doi: 10.1038/s41598-020-62118-4.

[2] Jorge Arroyo-Esquivel, Alyssa Gehman, Katie Collins, and Fernanda Sanchez. Managing populations after a disease outbreak: exploration of epidemiological consequences of managed host reintroduction following disease-driven host decline. *bioRxiv*, 2025. doi: 10.1101/2025.02.28.640833.

[3] AZA SAFE. Sunflower sea star program plan 2024–2027. Technical report, Association of Zoos and Aquariums, 2024.

[4] Amanda E. Bates, Brett J. Hilton, and Christopher D. G. Harley. Effects of temperature, season and locality on wasting disease in the keystone predatory sea star *Pisaster ochraceus*. *Diseases of Aquatic Organisms*, 86:245–251, 2009.

[5] Mark A. Beaumont, Jean-Marie Cornuet, Jean-Michel Marin, and Christian P. Robert. Adaptive approximate Bayesian computation. *Biometrika*, 96:983–990, 2009.

[6] Jenn M. Burt, M. Tim Tinker, Daniel K. Okamoto, Kyle W. Demes, Katie Holmes, and Anne K. Salomon. Sudden collapse of a mesopredator reveals its complementary role in mediating rocky reef regime shifts. *Proceedings of the Royal Society B*, 285:20180553, 2018. doi: 10.1098/rspb.2018.0553.

[7] Francesca Campolongo, Jessica Cariboni, and Andrea Saltelli. An effective screening design for sensitivity analysis of large models. *Environmental Modelling & Software*, 22 (10):1509–1518, 2007. doi: 10.1016/j.envsoft.2006.10.004.

[8] Matthew Clement, Rodrigo Hamede, Menna E. Jones, and Paul A. Hohenlohe. Coevolution enables host persistence in an eco-evolutionary epidemiological model of Tasmanian devil facial tumor disease. *Evolution*, 78(12):2095–2110, 2024. doi: 10.1093/evolut/qpae143.

[9] Matthew Clement et al. Eco-evolutionary individual-based model for coevolution between Tasmanian devils and devil facial tumour disease. *Evolution*, 2024. doi: 10.1093/evolut/qpae143.

[10] Renee M. Clouse and Ian Hewson. The 2022 *Diadema antillarum* mass mortality event: revisiting a Caribbean crisis. *Diseases of Aquatic Organisms*, 152:175–184, 2022.

[11] Donald L. DeAngelis and Wolf M. Mooij. Individual-based modeling of ecological and evolutionary processes. *Annual Review of Ecology, Evolution, and Systematics*, 36:147–168, 2005. doi: 10.1146/annurev.ecolsys.36.102003.152644.

[12] Morgan E. Eisenlord, Maya L. Groner, Robin M. Yoshioka, Jennifer Elliott, Jeffrey Maynard, Steven Fradkin, Margaret Turner, Katie Pyne, Sandy Wyllie-Echeverria, Benjamin G. Miner, and C. Drew Harvell. Ochre star mortality during the 2014 wasting disease epizootic: role of population size and temperature. *Philosophical Transactions of the Royal Society B*, 371(1689):20150212, 2016. doi: 10.1098/rstb.2015.0212.

[13] Bjarki Eldon and Wolfgang Stephan. Sweepstakes reproduction facilitates rapid adaptation in highly fecund populations. *Molecular Ecology*, 33:e16903, 2024. doi: 10.1111/mec.16903.

[14] Carolyn S. Friedman, Karl B. Andree, Kimberly A. Beauchamp, James D. Moore, Thea T. Robbins, Jeffrey D. Shields, and Ronald P. Hedrick. *Candidatus Xenohaliotis californiensis*, a newly described pathogen of abalone, *Haliotis* spp., along the west coast of North America. *International Journal of Systematic and Evolutionary Microbiology*, 50:847–855, 2000.

[15] Aaron W. E. Galloway, Sarah A. Gravem, Jenna N. Kobelt, et al. Sunflower sea star predation on urchins can facilitate kelp forest recovery. *Proceedings of the Royal Society B*, 290:20221897, 2023. doi: 10.1098/rspb.2022.1897.

[16] Joanna C. Gascoigne and Romuald N. Lipcius. Allee effects in marine systems. *Marine Ecology Progress Series*, 269:49–59, 2004. doi: 10.3354/meps269049.

[17] Alyssa-Lois M. Gehman, Olivier Pontier, Tanya Froese, Derek VanMaanen, Tristan Blaine, Gillian Sadlier-Brown, Alexis M. Olson, Zachary L. Monteith, Kiteria Bachen,

Christy Prentice, Margot Hessing-Lewis, and Jennifer M. Jackson. Fjord oceanographic dynamics provide refuge for critically endangered *Pycnopodia helianthoides*. *Proceedings of the Royal Society B*, 292:20242770, 2025. doi: 10.1098/rspb.2024.2770.

[18] Àlex Giménez-Romero, Antoni Grau, Iris E. Hendriks, and Manuel A. Matías. Modelling parasite-produced marine diseases: The case of the mass mortality event of *Pinna nobilis*. *Ecological Modelling*, 459:109740, 2021. doi: 10.1016/j.ecolmodel.2021.109740.

[19] Sarah A. Gravem and Bruce A. Menge. Metapopulation-scale resilience to disease-induced mass mortality in a keystone predator: From stasis to instability. *Ecosphere*, 16:e70426, 2025. doi: 10.1002/ecs2.70426.

[20] Sarah A. Gravem, Walter N. Heady, Vienna R. Saccomanno, Kathleen F. Alvstad, Alyssa-Lois M. Gehman, Taylor N. Frierson, and Scott L. Hamilton. *Pycnopodia helianthoides*. *The IUCN Red List of Threatened Species*, 2021. doi: 10.2305/IUCN.UK.2021-1.RLTS.T178290276A197818455.en.

[21] Volker Grimm and Steven F. Railsback. *Individual-Based Modeling and Ecology*. Princeton University Press, Princeton, NJ, 2005.

[22] Mary Hagedorn et al. Assisted gene flow using cryopreserved sperm in critically endangered coral. *Proceedings of the National Academy of Sciences*, 118:e2110559118, 2021. doi: 10.1073/pnas.2110559118.

[23] S. L. Hamilton, V. R. Saccomanno, W. N. Heady, A. L. Gehman, S. I. Lonhart, R. Beas-Luna, F. T. Francis, L. Lee, L. Rogers-Bennett, A. K. Salomon, and S. A. Gravem. Disease-driven mass mortality event leads to widespread extirpation and variable recovery potential of a marine predator across the eastern Pacific. *Proceedings of the Royal Society B*, 288:20211195, 2021. Alias for Hamilton2021.

[24] Scott L. Hamilton et al. Disease-driven mass mortality event leads to widespread extirpation and variable recovery potential of a marine predator across the eastern Pacific. *Proceedings of the Royal Society B*, 288:20211195, 2021. doi: 10.1098/rspb.2021.1195.

[25] C. Drew Harvell, Diego Montecino-Latorre, Joseph M. Caldwell, Jenn M. Burt, Kathryn Bosley, et al. Disease epidemic and a marine heat wave are associated with the continental-scale collapse of a pivotal predator (*Pycnopodia helianthoides*). *Science Advances*, 5:eaau7042, 2019. doi: 10.1126/sciadv.aau7042.

[26] C. Drew Harvell, Diego Montecino-Latorre, Joseph M. Caldwell, Jenn M. Burt, Kathryn Bosley, et al. Disease epidemic and a marine heat wave are associated with the

continental-scale collapse of a pivotal predator (*Pycnopodia helianthoides*). *Science Advances*, 5:eaau7042, 2019. doi: 10.1126/sciadv.aau7042.

[27] Dennis Hedgecock and Alexander I. Pudovkin. Sweepstakes reproductive success in highly fecund marine fish and shellfish: A review and commentary. *Bulletin of Marine Science*, 87:971–1002, 2011. doi: 10.5343/bms.2010.1051.

[28] Jon Herman and Will Usher. SALib: An open-source Python library for sensitivity analysis. *Journal of Open Source Software*, 2(9):97, 2017. doi: 10.21105/joss.00097.

[29] Ian Hewson. When bacteria meet many arms: Autecological insights into *Vibrio pectinicida* FHCF-3 in echinoderms. *bioRxiv*, 2025. doi: 10.1101/2025.08.15.670479.

[30] Ian Hewson, Jason B. Button, Brent M. Gudenkauf, et al. Densovirus associated with sea-star wasting disease and mass mortality. *Proceedings of the National Academy of Sciences*, 111:17278–17283, 2014. doi: 10.1073/pnas.1416625111.

[31] Ian Hewson, Citlalli A. Aquino, and Christiane M. DeRito. A scuticociliate causes mass mortality of *Diadema antillarum* in the Caribbean. *Science Advances*, 9:eadg3200, 2023.

[32] Ian Hewson, Morgan R. Johnson, and Benjamin Reyes-Chavez. Lessons learned from the sea star wasting disease investigation. *Annual Review of Marine Science*, 17:257–279, 2025. doi: 10.1146/annurev-marine-040623-082617.

[33] Ian Hewson et al. Investigating the complex association between viral ecology, environment, and Northeast Pacific sea star wasting. *Frontiers in Marine Science*, 5:77, 2018. doi: 10.3389/fmars.2018.00077.

[34] Ian Hewson et al. Perspective: Something old, something new? Review of wasting and other mortality in Asteroidea (Echinodermata). *Frontiers in Marine Science*, 6:406, 2019. doi: 10.3389/fmars.2019.00406.

[35] J. Hodin et al. A roadmap for the conservation of the sunflower sea star, *Pycnopodia helianthoides*. *Biological Conservation*, 2021. Alias for Hodin2021.

[36] Jason Hodin, Amanda Pearson-Lund, Freya P. Anteau, Philippe Kitaeff, and Sarah Cefalu. Progress toward complete life-cycle culturing of the endangered sunflower star, *Pycnopodia helianthoides*. *Biological Bulletin*, 241:243–258, 2021. doi: 10.1086/716552.

[37] Emmanuel Klinger, Dennis Rickert, and Jan Hasenauer. pyABC: distributed, likelihood-free inference. *Bioinformatics*, 34:3591–3593, 2018.

[38] C. Lambert, J.-L. Nicolas, V. Cilia, and S. Corre. Vibrio pectenicida sp. nov., a pathogen of scallop (Pecten maximus) larvae. *International Journal of Systematic Bacteriology*, 48:481–487, 1998. doi: 10.1099/00207713-48-2-481.

[39] Ryan E. Langendorf, James A. Estes, James C. Watson, Michael C. Kenner, Brian B. Hatfield, M. Tim Tinker, Elizabeth Waddle, Michelle L. DeMarch, and Daniel F. Doak. Dynamic and context-dependent keystone species effects in kelp forests. *Proceedings of the National Academy of Sciences*, 2025. doi: 10.1073/pnas.XXXXXXX.

[40] Harilaos A. Lessios. The great *Diadema antillarum* die-off: 30 years later. *Annual Review of Marine Science*, 8:267–283, 2016. doi: 10.1146/annurev-marine-122414-033857.

[41] Katie E. Lotterhos and Michael C. Whitlock. The relative power of genome scans to detect local adaptation depends on sampling design and statistical method. *Molecular Ecology*, 24(5):1031–1046, 2015. doi: 10.1111/mec.13100.

[42] Dayv Lowry, Sarah Wright, Melissa Neuman, et al. Endangered Species Act status review report: Sunflower sea star (*Pycnopodia helianthoides*). Technical report, NOAA National Marine Fisheries Service, 2022.

[43] Carolyn J. Lundquist and Louis W. Botsford. Model projections of the fishery implications of the Allee effect in broadcast spawners. *Ecological Applications*, 14:929–941, 2004. doi: 10.1890/02-5325.

[44] Coralie Lupo, Pedro J. Cabello-Yeves, Sara Ferreira, Julien de Lorgeril, and Luigi Vezzulli. Vibrio ecology, pathogenesis, and evolution. *Frontiers in Microbiology*, 11:587685, 2020. doi: 10.3389/fmicb.2020.587685.

[45] Coralie Lupo et al. Spatial epidemiological modelling of infection by *Vibrio aestuarianus* shows that connectivity and temperature control oyster mortality. *Aquaculture Environment Interactions*, 12:511–527, 2020. doi: 10.3354/aei00379.

[46] Michael Lynch. Evolution of the mutation rate. *Trends in Genetics*, 26:345–352, 2010. doi: 10.1016/j.tig.2010.05.003.

[47] Sara Meiling, Erinn M. Muller, Tyler B. Smith, and Marilyn E. Brandt. 3d photogrammetry reveals declining health of coral reefs during multi-year stony coral tissue loss disease outbreak. *Frontiers in Marine Science*, 8:631338, 2021.

[48] Zofia D. Meunier, Sally D. Hacker, and Bruce A. Menge. Regime shifts in rocky intertidal communities associated with a marine heatwave and disease outbreak. *Nature Ecology & Evolution*, 8:1285–1297, 2024. doi: 10.1038/s41559-024-02425-5.

[49] C. Melissa Miner, Jennifer L. Burnaford, Richard F. Ambrose, Liam Antrim, et al. Large-scale impacts of sea star wasting disease (SSWD) on intertidal sea stars and implications for recovery. *PLoS ONE*, 13:e0192870, 2018. doi: 10.1371/journal.pone.0192870.

[50] Diego Montecino-Latorre, Morgan E. Eisenlord, Marguerite Turner, Reyn Yoshioka, C. Drew Harvell, Christy V. Pattengill-Semmens, James D. Nichols, and Joseph K. Gaydos. Devastating transboundary impacts of sea star wasting disease on subtidal asteroids. *PLOS ONE*, 11:e0163190, 2016. Alias for Montecino-Latorre2016.

[51] Diego Montecino-Latorre, Morgan E. Eisenlord, Morgan Turner, Reyn Yoshioka, C. Drew Harvell, et al. Devastating transboundary impacts of sea star wasting disease on subtidal asteroids. *PLoS ONE*, 11:e0163190, 2016. doi: 10.1371/journal.pone.0163190.

[52] Diego Montecino-Latorre, Morgan E. Eisenlord, Morgan Turner, Reyn Yoshioka, C. Drew Harvell, et al. Devastating transboundary impacts of sea star wasting disease on subtidal asteroids. *PLoS ONE*, 11:e0163190, 2016. doi: 10.1371/journal.pone.0163190.

[53] Max D. Morris. Factorial sampling plans for preliminary computational experiments. *Technometrics*, 33(2):161–174, 1991. doi: 10.1080/00401706.1991.10484804.

[54] Laura D. Mydlarz, Laura E. Jones, and C. Drew Harvell. Innate immunity, environmental drivers, and disease ecology of marine and freshwater invertebrates. *Annual Review of Ecology, Evolution, and Systematics*, 37:251–288, 2006.

[55] NOAA National Centers for Environmental Information. NOAA optimum interpolation SST (OISST) version 2.1, 2020. URL `https://www.ncei.noaa.gov/products/optimum-interpolation-sst`.

[56] Melissa H. Pespeni and Lauren M. Schiebelhut. Insight into the genomic basis of disease resistance in a keystone sea star. *Molecular Ecology*, 32:5306–5320, 2023.

[57] Maya B. Prentice, Citlalli A. Aquino, Amy M. Chan, Kalia M. Davis, Paul K. Hershberger, Jan F. Finke, Jason Hodin, Aquiala McCracken, Christina T. E. Kellogg, Rute B. G. Clemente-Carvalho, Christy Prentice, Kiana X. Zhong, C. Drew Harvell, Curtis A. Suttle, and Alyssa-Lois M. Gehman. *Vibrio pectenicida* strain FHCF-3 is a causative agent of sea star wasting disease. *Nature Ecology & Evolution*, 2025. doi: 10.1038/s41559-025-02797-2.

[58] N. Prentice et al. Koch's postulates confirm *Vibrio pectenicida* as causative agent of sea star wasting disease in *Pycnopodia helianthoides*. *Nature Ecology & Evolution*, 2025. Alias for Prentice2025.

[59] Lars Råberg, Andrea L. Graham, and Andrew F. Read. Decomposing health: tolerance and resistance to parasites in animals. *Philosophical Transactions of the Royal Society B*, 364(1513):37–49, 2009. doi: 10.1098/rstb.2008.0184.

[60] Laura Rogers-Bennett and Cynthia A. Catton. Marine heat wave and multiple stressors tip bull kelp forest to sea urchin barrens. *Scientific Reports*, 9:15050, 2019. doi: 10.1038/s41598-019-51114-y.

[61] John Ryan. San juans' sea stars start long crawl back from near-extinction. KUOW, August 2024. URL `https://www.kuow.org/stories/san-juans-sea-stars-start-long-crawl-back-from-near-extinction`.

[62] Andrea Saltelli. Making best use of model evaluations to compute sensitivity indices. *Computer Physics Communications*, 145(2):280–297, 2002. doi: 10.1016/S0010-4655(02)00280-1.

[63] Andrea Saltelli, Marco Ratto, Terry Andres, Francesca Campolongo, Jessica Cariboni, Debora Gatelli, Michaela Saisana, and Stefano Tarantola. *Global Sensitivity Analysis: The Primer*. John Wiley & Sons, 2008. doi: 10.1002/9780470725184.

[64] Lauren M. Schiebelhut, Jonathan B. Puritz, and Michael N. Dawson. Decimation by sea star wasting disease and rapid genetic change in a keystone species, *Pisaster ochraceus*. *Proceedings of the National Academy of Sciences*, 115:7069–7074, 2018. doi: 10.1073/pnas.1800285115.

[65] Lauren M. Schiebelhut, Jonathan B. Puritz, and Michael N. Dawson. Decimation by sea star wasting disease and rapid genetic change in a keystone species, *Pisaster ochraceus*. *Proceedings of the National Academy of Sciences*, 115(27):7069–7074, 2018. doi: 10.1073/pnas.1800285115.

[66] Lauren M. Schiebelhut et al. A reference genome for ecological restoration of the sunflower sea star, *Pycnopodia helianthoides*. *Journal of Heredity*, 115:86–93, 2024. doi: 10.1093/jhered/esad054.

[67] L. Courtney Smith, Julie Ghosh, Katherine M. Buckley, Lori A. Clow, Nolwenn M. Dheilly, Tor Haug, John H. Henson, Chun Li, Cheng Man Lun, Audrey J. Majeske,

Valeria Matranga, Sham V. Nair, Jonathan P. Rast, David A. Raftos, Macey Roth, Stefano Sacchi, Catherine S. Schrankel, and Klara Stensvag. Echinoderm immunity. *Advances in Experimental Medicine and Biology*, 708:260–301, 2010.

[68] Il'ya M. Sobol'. Global sensitivity indices for nonlinear mathematical models and their Monte Carlo estimates. *Mathematics and Computers in Simulation*, 55(1–3):271–280, 2001. doi: 10.1016/S0378-4754(00)00270-6.

[69] Megumi F. Strathmann. *Reproduction and Development of Marine Invertebrates of the Northern Pacific Coast*. University of Washington Press, Seattle, 1987.

[70] Sunflower Star Laboratory. First temporary experimental outplanting of sunflower stars in California. SSL Press Release, December 2025. URL `https://www.sunflowerstarlab.org/news/sunflower-stars-restoration-research-california`.

[71] Stephen E. Swearer, Jeffrey S. Shima, Michael E. Hellberg, Simon R. Thorrold, Geoffrey P. Jones, D. Ross Robertson, Steven G. Morgan, Kimberly A. Selkoe, Gregory M. Ruiz, and Robert R. Warner. Evidence of self-recruitment in demersal marine populations. *Bulletin of Marine Science*, 70:251–271, 2002.

[72] Nick Tolimieri. Appendix A: Population viability analysis of *Pycnopodia helianthoides*. *In: Lowry et al., ESA Status Review Report, NOAA NMFS*, 2022.

[73] Tina Toni, David Welch, Natalja Strelkowa, Andreas Ipsen, and Michael P. H. Stumpf. Approximate Bayesian computation scheme for parameter inference and model selection in dynamical systems. *Journal of the Royal Society Interface*, 6:187–202, 2009.

[74] Helen J. Wearing, Pejman Rohani, and Matt J. Keeling. Appropriate models for the management of infectious diseases. *PLoS Medicine*, 2(7):e174, 2005. doi: 10.1371/journal.pmed.0020174.

A Supplementary Material

A.1 S1: Complete Parameter Table

Table 7 provides the complete specification of all 47 model parameters organized by functional group, including default values, sensitivity analysis ranges, confidence tier assignments (Tier 1: literature-constrained; Tier 2: informed priors; Tier 3: calibration targets), and primary source references. A comprehensive parameter justification report—including first-principles derivations, literature review of 103 sources, and quantitative interaction chain analysis across seven mechanistic pathways—is available as Supplementary Document S1 (`specs/parameter_justification/parameter_justification_report.pdf`).

Table 7: Complete parameter specification for SSWD-EvoEpi. Tiers: 1 = literature-constrained, 2 = informed prior, 3 = calibration target. SA ranges define uniform (U) or log-uniform (LU) sampling bounds.

Group	Parameter	Symbol	Default	SA Range	Tier	Source
Disease	E→I_1 rate	$\mu_{\text{EI1,ref}}$	$0.233\,\text{d}^{-1}$	[0.15, 0.35]	1	Prentice et al. [58]
Disease	I_1→I_2 rate	$\mu_{\text{I1I2,ref}}$	$0.434\,\text{d}^{-1}$	[0.25, 0.65]	1	Prentice et al. [58]
Disease	I_2→D rate	$\mu_{\text{I2D,ref}}$	$0.563\,\text{d}^{-1}$	[0.30, 0.85]	1	Prentice et al. [58]
[Remaining 44 parameters to be populated from sensitivity analysis parameter specification]						

A.2 S2: Sensitivity Analysis Details

S2.1: Morris R4 — Full Parameter Ranking

Table 8 presents the complete Morris elementary effects ranking for all 47 parameters across 23 output metrics, from the Round 4 analysis (960 runs, 11-node stepping-stone network, $K = 5{,}000$ per node, 20-year horizon).

Table 8: Full Morris R4 parameter ranking (47 parameters, 23 metrics). Only the top 10 are shown; see Supplementary Document S2 for the complete table.

Table placeholder: Complete Morris ranking table to be generated from `results/sensitivity_r4/` analysis outputs.

S2.2: Sobol R4 — Variance Decomposition

The Sobol variance decomposition ($N = 512$, 25,088 model evaluations) is in progress at time of writing. Results will include first-order (S_1) and total-order (S_T) indices for all 47 parameters across 23 metrics, with particular attention to the interaction gap $S_T - S_1$ and key pairwise interactions identified by the Morris screening: $\rho_{\text{rec}} \times \bar{c}_0$, $P_{\text{env,max}} \times a_{\text{exposure}}$, and $n_{\text{resistance}} \times \sigma_{v,\text{mut}}$.

S2.3: Sensitivity Analysis Figures

Figure placeholder: Morris μ^*–σ scatter plot for all 47 parameters, showing universal $\sigma/\mu^* > 1.0$ interaction dominance.

Figure 6: Morris μ^* vs. σ for all 47 parameters (R4).

Figure placeholder: Per-metric Morris importance heatmap (47 parameters × 23 metrics).

Figure 7: Morris importance heatmap across all metrics.

A.3 S3: Validation Details

S3.1: Per-Node Results ($K = 5{,}000$, R→S)

Detailed per-node trajectories and summary statistics for the baseline validation under biologically correct reinfection dynamics (sinusoidal and satellite SST forcing).

Table 9: Detailed per-node statistics under R→S ($K = 5{,}000$, sinusoidal SST): initial and final populations, peak infection prevalence, time to nadir, total infections, recoveries, disease deaths, and trait shifts at simulation end.

Table placeholder: Extended per-node validation results from `results/validation_rs_fix/`.

S3.2: Scale Dependence ($K = 100{,}000$)

Per-node results from the $K = 100{,}000$ validation run (permanent immunity; the R→S correction at this scale is pending).

Table 10: Per-node results at $K = 100{,}000$ (permanent immunity, sinusoidal SST).

Table placeholder: Extended $K = 100{,}000$ validation results.

S3.3: Validation Figures

Figure placeholder: Side-by-side population trajectories under permanent immunity vs. R→S, showing the dramatic impact of the reinfection correction.

Figure 8: Population trajectories: permanent immunity vs. R→S.

A.4 S4: Network Configuration

S4.1: Node Coordinates and Properties

Table 11: 11-node stepping-stone network configuration. Coordinates are approximate centroids of *Pycnopodia helianthoides* habitat. SST values are annual means from NOAA OISST v2.1 climatology (2002–2025).

#	Node	Lat	Lon	$\bar{T}$ (°C)	S (psu)	ϕ (d^{-1})
1	Sitka	57.06	−135.33	8.9	30.0	0.50
2	Ketchikan	55.34	−131.64	9.2	30.5	0.50
3	Haida Gwaii	53.25	−132.07	9.5	31.0	0.60
4	Bella Bella	52.16	−128.15	9.8	29.0	0.40
5	Howe Sound	49.38	−123.23	10.4	22.0	0.03
6	San Juan Isl.	48.53	−123.01	10.2	30.0	0.30
7	Westport	46.89	−124.10	11.0	33.0	0.80
8	Newport	44.63	−124.05	11.5	33.5	0.70
9	Crescent City	41.75	−124.20	12.0	33.0	0.70
10	Fort Bragg	39.45	−123.80	12.5	33.0	0.65
11	Monterey	36.62	−121.90	13.3	33.5	0.50

S4.2: Inter-Node Distances and Connectivity

Table 12: Pairwise overwater distances (km) and larval connectivity coefficients (C_{jk}) at $D_L = 400\,\text{km}$ for adjacent node pairs in the 11-node stepping-stone network.

Table placeholder: Pairwise distance and connectivity matrix.

A.5 S5: SST Climatology Data

Sea surface temperature forcing was derived from the NOAA Optimum Interpolation SST version 2.1 dataset [55], a 0.25° resolution global daily product. For each of the 11 network nodes, day-of-year climatological means were computed from 24 years of monthly data (2002–2025), accessed via the NOAA Physical Sciences Laboratory OPeNDAP server, and interpolated to daily resolution.

Figure placeholder: Daily SST climatology profiles for all 11 nodes, showing the latitudinal gradient from Sitka ($\bar{T} \approx 8.9$°C) to Monterey ($\bar{T} \approx 13.3$°C). Note asymmetric warming profiles and coastal upwelling signatures at exposed sites.

Figure 9: NOAA OISST v2.1 daily climatological SST profiles for the 11-node network.